Monthly Notices of the ROYAL ASTRONOMICAL SOCIETY

MNRAS **529,** 3323–3341 (2024) https://doi.org/10.1093/mnras/stae707
Advance Access publication 2024 March 8

Confronting compositional confusion through the characterization of the sub-Neptune orbiting HD 77946

L. Palethorpe [1,2]★ A. Anna John [3,4] A. Mortier [5] J. Davoult [6] T. G. Wilson [3,4] K. Rice [1,2] A. C. Cameron [3,4] Y. Alibert [6,7] L. A. Buchhave [8] L. Malavolta [9] J. Cadman [1,2] M. López-Morales [10] X. Dumusque [11] A. M. Silva [12,13] S. N. Quinn [10] V. Van Eylen [14] S. Vissapragada [10] L. Affer [15] D. Charbonneau [10] R. Cosentino [16] A. Ghedina [16] R. D. Haywood [17]† D. W. Latham [10] F. Lienhard [18] A. F. Martínez Fiorenzano [16] M. Pedani [16] F. Pepe,[11] M. Pinamonti [19] A. Sozzetti [19] M. Stalport [12] S. Udry [13] and A. Vanderburg [20]

Affiliations are listed at the end of the paper

Accepted 2024 March 5. Received 2024 March 1; in original form 2023 September 22

ABSTRACT

We report on the detailed characterization of the HD 77946 planetary system. HD 77946 is an F5 ($M_* = 1.17$ M$_\odot$, $R_* = 1.31$ R$_\odot$) star, which hosts a transiting planet recently discovered by NASA's *Transiting Exoplanet Survey Satellite* (*TESS*), classified as TOI-1778 b. Using *TESS* photometry, high-resolution spectroscopic data from HARPS-N, and photometry from *CHEOPS*, we measure the radius and mass from the transit and radial velocity observations, and find that the planet, HD 77946 b, orbits with period $P_b = 6.527282^{+0.000015}_{-0.000020}$ d, has a mass of $M_b = 8.38 \pm 1.32$ M$_\oplus$, and a radius of $R_b = 2.705^{+0.086}_{-0.081}R_\oplus$. From the combination of mass and radius measurements, and the stellar chemical composition, the planet properties suggest that HD 77946 b is a sub-Neptune with a ∼1 per cent H/He atmosphere. However, a degeneracy still exists between water-world and silicate/iron-hydrogen models, and even though interior structure modelling of this planet favours a sub-Neptune with a H/He layer that makes up a significant fraction of its radius, a water-world composition cannot be ruled out, as with $T_{eq} = 1248^{+40}_{-38}$ K, water may be in a supercritical state. The characterization of HD 77946 b, adding to the small sample of well-characterized sub-Neptunes, is an important step forwards on our journey to understanding planetary formation and evolution pathways. Furthermore, HD 77946 b has one of the highest transmission spectroscopic metrics for small planets orbiting hot stars, thus transmission spectroscopy of this key planet could prove vital for constraining the compositional confusion that currently surrounds small exoplanets.

Key words: techniques: photometric – techniques: radial velocities – techniques: spectroscopic – planets and satellites: composition – planets and satellites: fundamental parameters – stars: individual (HD 77946).

1 INTRODUCTION

The *Transiting Exoplanet Survey Satellite* (*TESS*) (Ricker et al. 2014), launched in 2018 April, has discovered thousands of planetary candidates in the half a decade its been operating and led to many precise planetary radius measurements. The *CHaracterising ExOPlanet Satellite* (*CHEOPS*) (Benz et al. 2021), launched in 2019 December, has allowed us to carry out follow-up observations of many *TESS* candidates, using ultra-high precision photometry on the bright stars already known to host planets. However, to determine these planets' bulk compositions, and thus constrain planetary formation and evolution pathways, precise measurements of their masses are also needed. For small transiting planets, dynamical techniques or high-precision spectra from ground-based instruments are commonly used. Examples of such instruments include the High Accuracy Radial Velocity Planet Searcher (HARPS) spectrograph hosted by the European Southern Observatory (ESO) 3.6 m telescope in Chile (Mayor et al. 2003); and its Northern hemisphere counterpart, HARPS-N, on the Italian 3.58 m Telescopio Nazionale Galileo on La Palma Island (Cosentino et al. 2012). Both HARPS and HARPS-N have been shown to have short-term precisions of ∼30 cm s^{-1} and sub-m s^{-1} precisions over time-scales of months (Cosentino et al. 2014).

The 'radius valley' that separates super-Earths and sub-Neptunes has been consistently observed at ∼1.5–2 R$_\oplus$ (Fulton et al. 2017; Fulton & Petigura 2018; Van Eylen et al. 2018; Ho & Eylen 2023), and is largely without planets. Debate currently surrounds the origin of this gap, with proposed scenarios including core-powered mass-loss, photoevaporation, or that these planets are primordially rocky. Interpretations differ on the physical mechanism of atmospheric mass-loss, but the result is the same – primordially accreted atmospheres are removed in such a way that different planets are affected in different ways over different time-scales, resulting in

★ E-mail: larissa.palethorpe@ed.ac.uk
† STFC Ernest Rutherford Fellow.

a valley which separates a population of stripped-core planets (super-Earths) from those which have retained their H/He envelopes (sub-Neptunes) (Owen & Wu 2013; Ginzburg, Schlichting & Sari 2018; Gupta & Schlichting 2019). While investigations have been launched into the existence of planets in the valley, it is still not immediately clear if there are any firm detections of planets in the gap. Larger population studies have indicated that at least a few planets fall within the radius valley, but conversely smaller and more precise planet samples have revealed a complete lack of planets across the gap (Ho & Eylen 2023). It has been observed, however, that the valley varies with planetary orbital separation, system age, and mass and metallicity of the host stars, which is consistent with the predictions of atmospheric mass-loss models (David et al. 2021; Sandoval, Contardo & David 2021; Petigura et al. 2022).

The internal structure of sub-Neptunes is not just limited to that of a rocky core surrounded by a gaseous atmosphere, it has been theorized that these planets might hold significant fractions of ices or liquid water (Rogers & Seager 2010; Dorn et al. 2017). Zeng et al. (2021) suggested that the radii of planets hotter than 900 K and with masses below 20 $M_\oplus$ can be reproduced assuming ice-dominated compositions without significant gaseous envelopes. The entire mass–radius (M-R) distribution of planets around the radius valley could therefore be separated into three groups: purely rocky planets, gas-poor water worlds, and gas-rich water worlds, where the first two represent the two peaks in the radius distribution (Luque & Pallé 2022). However, Rogers, Schlichting & Owen (2023) argue that the existence of small planets with hydrogen atmospheres are consistent with the data, once thermal evolution and mass-loss are properly accounted for. This means that there is a strong degeneracy between water-world and silicate/iron-hydrogen models, and that the characterization of larger sub-Neptunes that reside in this area of the M-R diagram can be used to determine planetary evolution and formation pathways (Kubyshkina & Fossati 2022).

Here, we present the analysis of the *TESS* target HD 77 946 (also known as TIC39699648, HIP 44746). We gathered radial velocity (RV) data from HARPS-N, as well as photometric data from *CHEOPS* and *TESS*, to measure its mass and radius and interpret its composition and investigate whether it meets current radius valley and compositional expectations. Currently, only about ∼11 per cent of sub-Neptunes have a measured mass, due to the difficulty in measuring their small RV signals (Kubyshkina & Fossati 2022). In this paper we add a significant contribution to this tiny sample of well-characterized small planets.

The paper is organized as follows. In Section 2, we detail the *TESS* and *CHEOPS* transit observations, and the HARPS-N RV observations. In Section 3, we derive the parameters of the host star, by combining high-resolution spectra with other sources of ancillary information. In Section 4, we describe the approach to modelling the HD 77 946 planetary system. In Section 5, we show the resulting properties of HD 77 946 b and discuss its composition in comparison to radius valley predictions and current compositional theories. Then to conclude, in Section 6, we provide a brief summary and final conclusions.

2 OBSERVATIONS

2.1 Photometry

2.1.1 TESS

HD 77 946 (also known as TOI-1778) was observed first by *TESS* in sector 21 (year 2) of its primary mission (Ricker et al. 2014), between

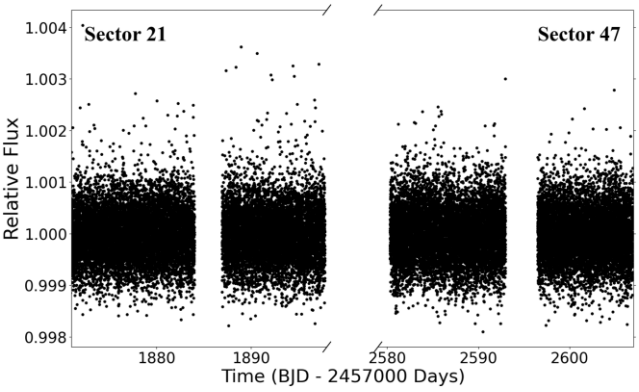

Figure 1. *TESS* photometry of HD 77 946 from sectors 21 and 47. The figure shows the PDCSAP *TESS* light curve where systematic errors have been removed, but the resulting light curve has not been corrected for low-frequency variations such as stellar activity.

UTC 2020 January 21 and UTC 2020 February 18 (BJD 2458870.43 and BJD 2458897.78, respectively). At this point TOI-1778.01 was identified as a *TESS* Object of Interest (TOI), due to a possible transiting planet identified by the Science Processing Operations Center/Transiting Planet Search (SPOC/TPS) pipeline as outlined in Guerrero et al. (2021). The SPOC pipeline (Jenkins et al. 2016) detected a candidate planetary signal with a period of 6.52 d, which was verified by a classification algorithm (*TESS*-ExoClass (TEC)[1]) and then vetted by the *TESS* team, thus promoting it to TOI status. The target was then re-observed during the *TESS* extended mission in sector 47 (year 4) between UTC 2021 December 30 and UTC 2022 January 28 (BJD 2459579.80 and BJD 2459600.95). Over a total of 54.8 d, *TESS* obtained 39 238 images of the target with 2 min cadence. The data observed in sector 21 were taken on CCD 2 of camera 1, while the data observed in sector 47 were taken on CCD 1 of camera 1. The data were reduced by the *TESS* data processing pipeline developed by the SPOC (Jenkins et al. 2016), which identified a total of seven transits of TOI-1778.01 over the 54.8 d baseline, with a signal-to-noise ratio (SNR) of 15.7 over both sectors.

For the photometric analysis, we downloaded the *TESS* photometry from the Mikulski Archive for Space Telescopes (MAST)[2] and started our analysis using the Pre-search Data Conditioning Simple Aperture Photometry (PDCSAP) light curve reduced by the SPOC. In the initial Simple Aperture Photometry (SAP) flux, a 0.94 d gap exists in sector 21, between BJD 2458884.00 and BJD 2458884.94, as well as a 0.97 d gap in sector 47, between BJD 2459592.96 and BJD 2459593.93. Both of these are due to telescope reorientation for transmission of data. This caused spikes in the SAP flux immediately after the telescope reorientation, between BJD 2458884.94 and BJD 2458886.92, and BJD 2459593.93 and BJD 2459596.48, respectively. These gaps and subsequent spikes were removed when deriving the PDCSAP light curve. Hence, the remaining PDCSAP light curve, shown in Fig. 1, contains a 2.92 d gap between BJD 2458884.00 and BJD 2458886.92, and a 3.52 d gap between BJD 2459592.96 and BJD 2459596.48. Throughout the remainder of this work we use the PDCSAP fluxes for determining any stellar and planetary signals.

In Section 4.1, we describe our approach to the modelling of the *TESS* photometry.

[1] https://github.com/christopherburke/TESS-ExoClass
[2] https://mast.stsci.edu/portal/Mashup/Clients/Mast/Portal.html

Table 1. Log of *CHEOPS* Observations of HD 77 946 b. The column T_{exp} gives the exposure time in terms of the integration time per image multiplied by the number of images stacked on-board prior to download. N_{obs} is the number of frames. Effic. is the proportion of the time in which unobstructed observations of the target occurred. R_{ap} is the aperture radius used for the photometric extraction. RMS is the standard deviation of the residuals from the best fit. The variables in the final column are as follows: time, t; spacecraft roll angle, ϕ, PSF centroid position, (x, y); smear correction, `smear`; aperture contamination, `contam`; image background level, `bg`.

Start date (UTC)	Duration (h)	T_{exp}	N_{obs}	Effic. (per cent)	File key	APER	R_{ap} (pixels)	RMS (ppm)	Decorrelation
2022-01-07T14:06	15.89	1 x 30 s	1064	56	CH_PR220007 _TG001301_V0200	OPTIMAL	25	1656	$\sin(\phi)$, $\cos(\phi)$, $\sin(2\phi)$, $\cos(2\phi)$
2022-12-06T10:42	16.77	1 x 30 s	1096	54	CH_PR220007 _TG001401_V0200	OPTIMAL	25	785	t, t^2, x, y, $\sin(\phi)$, $\cos(\phi)$, $\sin(2\phi)$, $\cos(2\phi)$, $\sin(3\phi)$, $\cos(3\phi)$, `contam`, `smear`, `bg`

2.1.2 CHEOPS

The *CHEOPS* spacecraft (Benz et al. 2021) was launched in 2019 to conduct ultra-high precision photometry to both aid in the discovery of new planets (Leleu et al. 2021; Osborn et al. 2022; Serrano et al. 2022; Wilson et al. 2022) and refine their properties (Bonfanti et al. 2021; Delrez et al. 2021; Lacedelli et al. 2022). To confirm and characterize the planet in the HD 77 946 system we obtained two visits of a transit of planet b within the *CHEOPS* AO-2 Guest Observers programme ID:07 (PI: Mortier), with the log of these observations presented in Table 1.

The data were processed using the *CHEOPS* Data Reduction Pipeline (DRP v13; Hoyer et al. 2020) that conducts frame calibration, instrumental and environmental correction, and aperture photometry using pre-defined radii (R = 22.5″[RINF], 25.0″[DEFAULT], 30.0″[RSUP], and OPTIMAL radius) as well as a noise-optimized radius [ROPT]. The size of the OPTIMAL radius is determined on a per-visit basis to account for the differing brightnesses of different targets, and is determined by minimizing the SNR (Hoyer et al. 2020). Both visits of HD 77 946 have the same optimized aperture radius of 25 pixels. The DRP produced flux contamination (see Hoyer et al. 2020 and Wilson et al. 2022 for computation and usage) that was subtracted from the light curves. We retrieved the data and corresponding instrumental basis vectors, assessed the quality using the PYCHEOPS Python package (Maxted et al. 2022), and decorrelated with the parameters suggested by this package, which can be found in Table 1. Outliers were also trimmed from the light curves, with points that were 4σ away from the median value removed. We concluded that using the OPTIMAL radius was the best option as it gave the highest SNR. Therefore, we used these detrended data, shown in Fig. 2, for further analysis.

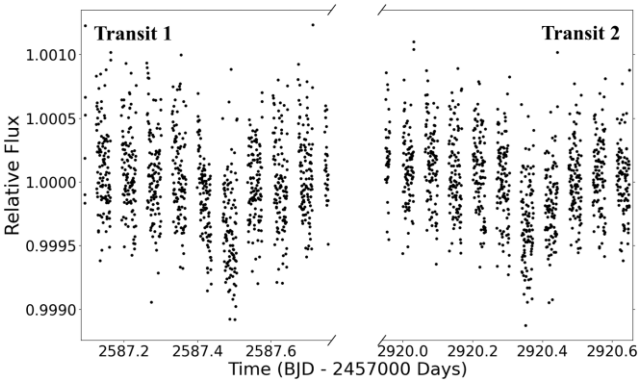

Figure 2. *CHEOPS* photometry of HD 77 946 from the two transits observed. The figure shows the *CHEOPS* light curves which have been decorrelated with the parameters in Table 1.

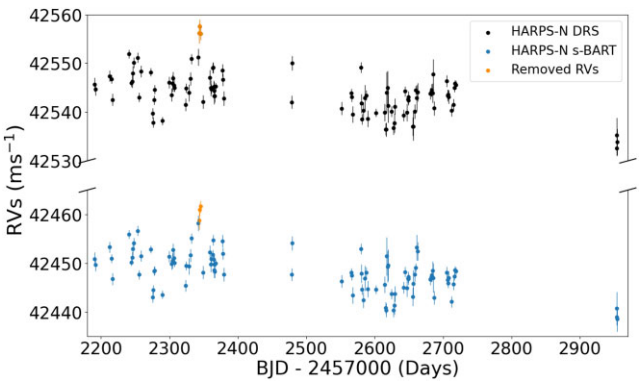

Figure 3. The HARPS-N DRS and s-BART RVs plotted against time. The DRS reduced RVs are plotted in black, while the s-BART reduced RVs are plotted in blue. The same three observations in both data sets, which were removed due to issues with the autoguider, are highlighted in orange.

2.2 HARPS-N spectroscopy

We collected 102 spectra for HD 77 946 with the HARPS-N high-resolution spectrograph (R = 115 000) (Cosentino et al. 2012) installed on the 3.6 m Telescopio Nazionale Galileo at the Observatorio de los Muchachos in La Palma, Spain. HARPS-N observed HD 77 946 between UTC 2020 December and UTC 2023 January (BJD 2459190.74 and BJD 2459954.68) as part of the HARPS-N Collaboration's Guaranteed Time Observations (GTO) programme. Our observational strategy initially consisted of taking one observation per night, lasting 15 min, for several consecutive nights in order to sample the RV curve of the transiting planet, and at later times performed more sporadic observations where we aimed to sample less well-resolved sections of the planet's orbital phase. The sampling strategy is shown in Fig. 3, along with the two different methods used to reduce the spectra and their resultant RVs, as explained in Sections 2.2.1 and 2.2.2. HD 77 946 is a bright star, with V-band magnitude V=8.99 ± 0.03, hence exposure times of 900s per observation were sufficient.

The obtained spectra had SNRs in the range 33–152 (average SNR = 91). We eliminated three observations, taken on consecutive nights BJD=2459343.44, 2459344.46, 2459345.46, due to an issue with the guiding component of HARPS-N which resulted in an anomalous offset and was confirmed in our well-observed standard stars. The removal of these RVs slightly increased the SNR (average SNR = 92), but did not change the average RV precision. Additionally, in UTC 2021 October the cryostat on the instrument was replaced leading to

an offset between the two seasons, which was accounted for when modelling the data.

2.2.1 DRS

The spectra were reduced using version 2.3.5 of the HARPS-N Data Reduction Software (DRS; Dumusque et al. 2021), with a G2 mask used in the cross-correlation function (CCF). The spectra obtained resulted in an average RV precision of 1.4 $m\,s^{-1}$ and an RMS of 4.44 $m\,s^{-1}$. The HARPS-N DRS data are presented in Table B1 which includes the RVs as well as the activity indicators: full width at half-maximum (FWHM) of the CCF, the line Bisector Inverse Slope (BIS), and the log R'_{HK} converted from the S-index following Noyes et al. (1984a).

2.2.2 s-BART

Following the confident detection of the transiting planet with the DRS RVs, the s-BART (Silva et al. 2022) template-matching pipeline was applied to the same data set. This approach is built around the core assumption that the RV signal introduced by the presence of an orbiting planet should be achromatic, i.e. independent of the wavelength at which it is measured. Telluric features are accounted for through a binary mask that rejects any wavelength for which Earth's transmittance drops under 1 per cent of its continuum value, which is enlarged to consider the BERV motion. Furthermore, to ensure that each observation is informed by the same wavelength region, s-BART only uses the spectral orders that are common to all observations in the data set. This model was implemented in a Bayesian framework, allowing for a straightforward and consistent characterization of the uncertainties associated with the RV extraction, and has been yielding good results for both ESPRESSO data (e.g. Faria et al. 2022) and HARPS-N (Wilson et al. 2024). This resulted in an average RV precision of 1.4 $m\,s^{-1}$ and an RMS of 4.45 $m\,s^{-1}$. The HARPS-N s-BART data are presented in Table B2.

3 STELLAR PARAMETERS

3.1 Atmospheric parameters

Two independent methods were employed to determine the stellar atmospheric parameters using the high-resolution HARPS-N spectra, namely ARES + MOOG and Stellar Parameter Classification (SPC).

The ARES + MOOG method, described in detail in Sousa (2014), determines the stellar parameters using the equivalent widths (EWs) of a series of iron absorption lines. For this analysis, all of the HARPS-N spectra were stacked together to create a very high-SNR spectrum. The EWs of a list of neutral and ionized iron absorption lines (Sousa et al. 2011) are automatically measured using the ARESV2 code (Sousa et al. 2015). The EWs are then fed into the 2017 version of the radiative transfer code MOOG (Sneden 1973) where iron abundances are compared to a grid of Kurucz Atlas 9 plane parallel model atmospheres (Kurucz 1993), which assume local thermodynamic equilibrium (LTE). The appropriate atmospheric model is determined through a minimization process (Press et al. 1992), from which the best-fitting stellar parameters are obtained. Derived values for $\log(g)$ were subsequently corrected following the method described in Mortier et al. (2014), and our errors were inflated to account for statistical tension by adding our precision errors and systematic errors in quadrature. We determined values $T_{\rm eff} = 6154 \pm 81$ K, $\log(g) = 4.41 \pm 0.11$, and [Fe/H] = 0.24 ± 0.06. Using these atmospheric parameters, we further used ARES + MOOG to derive individual elemental abundances for magnesium and silicon. These elemental abundances, in combination with the iron abundance, can be used to derive the planet's interior composition. Details of the method and line list are found in Mortier et al. (2013). We ran MOOG again in LTE mode and the values of Asplund et al. (2009) were used as a reference for the solar values.

By comparison SPC, described in detail in Buchhave et al. (2012, 2014), is a spectral synthesis method. In this method, each HARPS-N spectrum is analysed individually and final stellar parameters are calculated as the average of each individual result weighted by their SNR. The value for $\log(g)$ is additionally constrained using isochrones. Again, our precision errors and systematic errors are added in quadrature. We obtained values $T_{\rm eff} = 5937 \pm 49$ K, $\log(g) = 4.20 \pm 0.10$, [m/H] $= 0.12 \pm 0.08$. We note that the iron abundance derived by this method is similar to an overall metallicity due to the abundance of iron lines in an optical spectrum.

Our final parameters adopted here, displayed in Table 2, are the average of the two methods. We used a Monte Carlo approach, using 100 000 samples to generate random Gaussian distributions of the three relevant parameters. An average distribution was then computed for each parameter from which the mean and standard deviation are taken as the final adopted atmospheric parameters.

We calculate the U, V, and W Galactic velocities using the method of Johnson & Soderblom (1987) and data from the most recent *Gaia* data release (for examples see Mortier et al. 2020 and Wilson et al. 2022), and compute the thin and thick disc, and halo membership probabilities. This was done using the framework outlined in Wilson et al. (2024) (in review), which combines new *Gaia* offset-corrected (Lindegren et al. 2021) data (Gaia Collaboration 2023) with a known probability method (Reddy, Lambert & Allende Prieto 2006), then uses a novel Monte Carlo approach to compute a weighted average combination of probabilities using four sets of velocity standards (Bensby, Feltzing & Lundström 2003; Reddy et al. 2006; Bensby, Feltzing & Oey 2014; Chen et al. 2021) corrected for the Local Standard of Rest (Koval, Marsakov & Borkova 2009). We find U = 44.66 ± 0.27 km s^{-1}, $V = -2.36 \pm 0.05$ km s^{-1}, and $W = 12.88 \pm 0.25$ km s^{-1}, resulting in 98.5 per cent, 1. per cent, and 0 per cent thin disc, thick disc, and halo probabilities, respectively, which is in line with the given metallicity for this type of star.

3.2 Stellar mass, radius, and age

Stellar parameters of HD 77 946 were determined using `isochrones` and stellar evolution tracks. For a detailed discussion on this see Mortier et al. (2020). In brief, spectroscopically determined values for the effective temperature and metallicity from ARES + MOOG and SPC were used as inputs to the `isochrones` python package (Morton 2015), together with the *Gaia* Early Data Release 3 (Brown et al. 2021) parallax and the apparent magnitude in eight bands, listed in Table 2. Two sets of stellar evolution models were used, the Dartmouth Stellar Evolution Database (Dotter et al. 2008) and the MESA Isochrones and Stellar Tracks (MIST - Dotter 2016). For each stellar evolution model (Dartmouth/MIST) the analysis was run twice; once using each of the spectroscopic inputs (ARES + MOOG/SPC), totalling to four individual runs. Final values for the stellar mass, radius, and age were obtained by combining the posteriors from each run, and taking the median and the 16th and 84th percentile. We derived values $M_* = 1.17^{+0.06}_{-0.05}$ M$_\odot$, $R_* = 1.31 \pm 0.01$ R$_\odot$, and $t_* = 3.85^{+1.26}_{-1.61}$ Gyr. Combining the derived mass and radius, we can compute a new value for the surface gravity,

Table 2. Stellar parameters for HD 77946.

Parameter	Value	Source
Name		
2MASS	*J*09070675+4640214	2MASS
Gaia DR3	1011 435 012 611 767 552	*Gaia* DR3 (2023)
HD	77 946	Nesterov et al. (1995)
HIP	44 746	Perryman et al. (1997)
TIC	39 699 648	Stassun et al. (2018)
TOI	1778	Guerrero et al. (2021)
TYC	3424 − 01533 − 1	Tycho-2
WISE	*J*090706.66+464020.9	*WISE*
Photometry		
RA	09:07:06.63	*Gaia* DR3 (2023)
Declination	+ 46:40:20.73	*Gaia* DR3 (2023)
π [mas]	10.07 ± 0.02	*Gaia* DR3 (2023)
d [pc]	$99.0^{+0.3}_{-0.2}$	Bailer-Jones et al. (2021)
log $R'_{\rm HK}$	-5.01 ± 0.05	This work
$P_{\rm rot}$ [d]	14 ± 2	This work
RV [m s^{-1}]	$2.22^{+0.06}_{-0.21}$	This work
U [km s^{-1}]	$+44.66 \pm 0.27$	This work
V [km s^{-1}]	-2.36 ± 0.05	This work
W [km s^{-1}]	$+12.88 \pm 0.25$	This work
Spectral Type	F5	Cannon & Pickering (1993)
B [mag]	9.59 ± 0.02	Tycho-2
V [mag]	9.00 ± 0.02	Tycho-2
J [mag]	7.904 ± 0.02	2MASS
H [mag]	7.67 ± 0.02	2MASS
K [mag]	7.62 ± 0.02	2MASS
$W1$ [mag]	7.56 ± 0.03	*WISE*
$W2$ [mag]	7.64 ± 0.02	*WISE*
$W3$ [mag]	7.62 ± 0.02	*WISE*
Atmospheric parameters		
$T_{\rm eff}$ [K]	6154 ± 81	ARES + MOOG
log$g$ [cgs]	4.41 ± 0.11	ARES + MOOG
[Fe/H]	0.24 ± 0.06	ARES + MOOG
[Mg/H]	0.41 ± 0.22	ARES + MOOG
[Si/H]	0.31 ± 0.08	ARES + MOOG
ξ_t [km s^{-1}]	1.42 ± 0.07	ARES + MOOG
$T_{\rm eff}$ [K]	5937 ± 49	SPC
log$g$ [cgs]	4.20 ± 0.10	SPC
[m/H]	0.12 ± 0.08	SPC
$v$sin$i$ [km s^{-1}]	3.5 ± 0.5	SPC
Adopted average parameters		
$T_{\rm eff}$ [K]	6046 ± 50	ARES + MOOG/SPC
log$g$ [cgs]	4.30 ± 0.07	ARES + MOOG/SPC
[m/H]	0.18 ± 0.05	ARES + MOOG/SPC
Stellar mass, radius, and age		
M_* [M$_\odot$]	$1.17^{+0.06}_{-0.05}$	`isochrones`
R_* [R$_\odot$]	1.31 ± 0.01	`isochrones`
t_* [Gyr]	$3.85^{+1.26}_{-1.61}$	`isochrones`
log$g$ [cgs]	$4.27^{+0.03}_{-0.02}$	`isochrones`

which is consistent with, but more precise than the spectroscopic surface gravity.

3.3 Stellar activity and rotation

Signals intrinsic to stars themselves still pose significant problems, as they can induce RV variations that can drown out or even mimic planetary signals (Rajpaul et al. 2021). Modelling and thus mitigating these signals is notoriously difficult. However, a technique that has proved successful for disentangling stellar activity signals from planetary signals is to use a Gaussian Process (GP) framework (Haywood et al. 2014; Rajpaul et al. 2015; Stock et al. 2020). GPs have a number of features that make them very well suited to the joint modelling of activity processes and dynamical (e.g. planetary) signals, giving probabilistic estimates of the model parameters, which leads to more precise and accurate mass estimates.

In addition to providing us with RVs, the HARPS-N spectra can be used to infer information about stellar activity. If it is observed that there is a significant stellar activity signal present in the RVs, then including a GP model in the RV fit is advised. We performed a Bayesian generalized Lomb–Scargle (BGLS) (Boisse et al. 2011; Mortier et al. 2015) analysis on the HARPS-N RVs, RV residuals (where the signal of the transiting planet has been subtracted), and each of the activity parameters, as well as the *TESS* SAP, shown in Fig. 4, in order to ascertain whether this was the case.

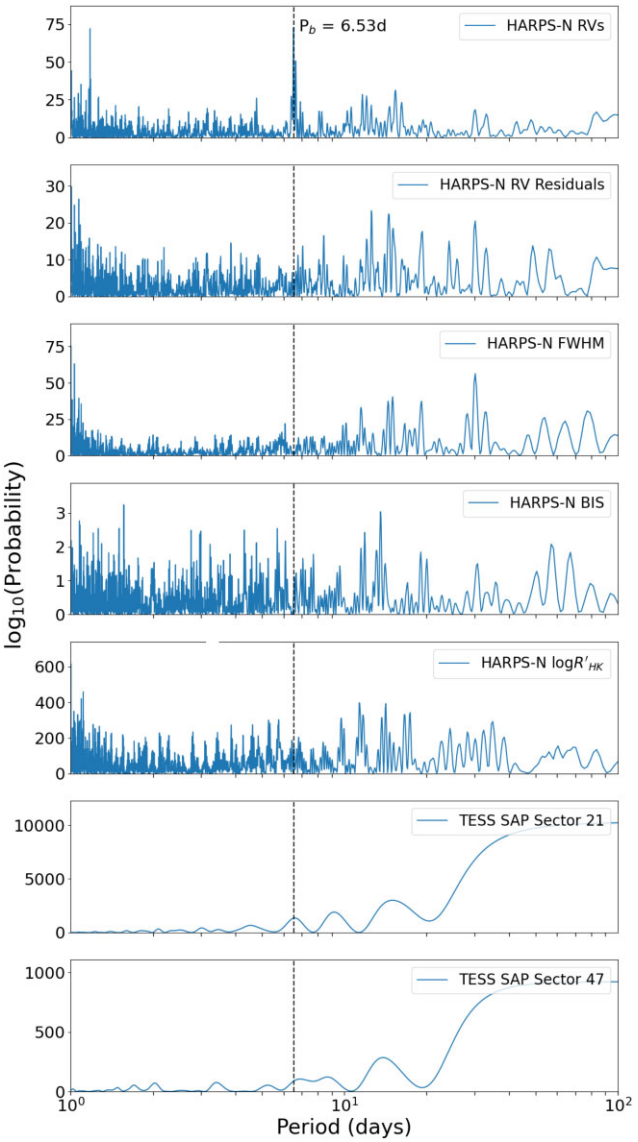

Figure 4. BGLS periodograms calculated using the HARPS-N RVs (first), the RV residuals (second), the FWHMs of the CCF (third), the BIS (fourth), the $S_{\rm HK}$ index (fifth), and the SAP from the two *TESS* sectors (sixth and seventh). The labelled dashed line shows the period of the transiting planet at 6.53 d.

The signal of the transiting planet (P_b) at 6.53 d is clearly visible from the RV values from HARPS-N (first panel of Fig. 4, highlighted by the labelled black dashed line) and *TESS* SAP (sixth and seventh panels of Fig. 4), with no corresponding signal in the RV residuals, FWHM, BIS, or log R'_{HK} values. While the absence of signals in activity indicators does not necessarily imply that the signal is not of stellar origin (Collier Cameron et al. 2019), this signal can be verified to be that of the planet as it is consistent with the P_b derived from both the *TESS* and *CHEOPS* photometry. While a definitive stellar activity signal was not identified in the stellar activity indicators presented in Fig. 4, there is a forest of peaks in the 10–20 d period range which may be indicative of stellar activity. The activity indicators can be sensitive to different types of variability, however, so peaks at the same period in multiple panels are not necessarily correlated. Hence it was deemed to be necessary to include a quasi-periodic GP regression model in the RV fit. A GP model was not used on the *TESS* data as the light curves are too short and any long-term trends greater than length of the *TESS* sector would then be excluded.

The S-index and associated log R'_{HK} are traditionally seen as an excellent indicator for a star's magnetic cycle. The Sun, for example, has an S-index varying between 0.16 and 0.18 throughout its 11-yr magnetic cycle (Egeland et al. 2017). The average log $R'_{HK} = -5.01 \pm 0.05$ for HD 77946, which would indicate a rotation period of ∼18 d using the calibrations from Noyes, Weiss & Vaughan (1984b), and a similar rotation period of ∼19 d and age of 3.5 Gyr using the calibrations from Mamajek & Hillenbrand (2008). However, these calibration relations are just estimates and a manifestation of the rotation period in the data may not be the same as the physical rotation period (Nava et al. 2020). The average value of log R'_{HK} can additionally be used to estimate the expected stellar-induced RV variations. From equation (1) of Hojjatpanah et al. (2020), a value of −5.01 for log R'_{HK} translates to an RV rms of $2.22^{+0.06}_{-0.21}$ m s^{-1}. In contrast, Suárez Mascareño et al. (2017) estimate the RV semi-amplitude induced by stellar activity variations of an F star with average log R'_{HK} of −5.01 should be lower than 1 m s^{-1}, though this was based on a smaller sample. HARPS-N solar data show an rms of 1.63 m s^{-1} (Collier Cameron et al. 2019) while the Sun was approaching solar minimum with values of log R'_{HK} around −4.97, thus we can expect RV variations from stellar activity at the level of 0.5–3 m s^{-1}.

There is a risk that when a model is used to try and constrain the planetary mass, some of the stellar activity is also modelled, resulting in a mass much higher or lower than the true value (Nava et al. 2022). Collier Cameron et al. (2021) developed an algorithm called SCALPELS to combat this problem, by separating the stellar RV variability component driven by spectral line-shape changes while preserving the planetary shift signals (Wilson et al. 2022). We used the TWEAKS pipeline, described in Anna John, Collier Cameron & Wilson (2022) and Anna John et al. (2023), for performing the stellar activity mitigation in the wavelength and time domain simultaneously. This is achieved by incorporating the SCALPELS basis vectors representing the shape components in the nested sampling package called KIMA[3] (Faria et al. 2018) for stellar activity decorrelation. As Anna John et al. (2022) have found, some shift-like signals elude SCALPELS analysis, so any remaining rotationally modulated signals were modelled with GP regression applied to the RVs.

We used a quasi-periodic GP kernel, which has four hyperparameters (θ, h, ω, λ) and is described by

$$\Sigma_{i,j} = h^2 \exp\left\{ -\frac{\sin^2[\pi(t_i - t_j)/\theta]}{2\omega^2} - \left(\frac{t_i - t_j}{\lambda}\right)^2 \right\}, \quad (1)$$

where t_i and t_j are two times of observation, and the other terms are the variability period of the star ($\theta = P_{rot}$), the variability amplitude ($h = H_{amp}$), the periodic characteristic length (associated with the number of spots/spot regions on the surface of the star, $\omega = O_{amp}$), and the non-periodic characteristic length (associated with the spot decay time-scale, λ). The GP was run with log-uniform priors on the amplitude $0 < \ln(h) < 2.7$ and active-region evolution time-scale 24 d $< \lambda <$ 40 d. These boundaries were selected based on the stellar type of HD 77946, an F dwarf, so we assume its active regions evolve on approximately the same time-scale as the Sun. The SPC gives $v \sin i = 3.5 \pm 0.5$ km s^{-1}, and based on a stellar radius of 1.31 $R_\odot$ this limits the stellar rotation period to a value of below 22 d. Based on this estimate and a few initial runs with uninformative priors, the GP priors on the stellar rotation period were set to be uniform with 12 d $< \theta <$ 19 d. The log harmonic complexity was controlled with a uniform prior $-1 < \ln(\omega) < 0$. In short, we used a model with up to five unknown Keplerian signals to maximize exploration, and stellar activity decorrelation performed against the SCALPELS basis vectors, incorporated with a quasi-periodic GP regression.

The joint posteriors showed clear detection of a Keplerian signal at orbital period ∼6.52 d, as well as identified a stellar rotation of $P_{rot} = 13.48^{+0.98}_{-0.42}$ d. From this investigation with the SCALPELS algorithm, we were able to place a prior on P_{rot} of $\mathcal{N}(14.0, 2.0)$ with a boundary of 10–20 d (determined from the activity signals in Fig. 4) for the joint fit with the photometric data, RV data, and the GP. This means that the stellar activity could be properly accounted for and the planetary mass correctly constrained.

4 PLANET MODELLING

4.1 Joint transit and RV modelling

To calculate the best-fitting planetary and stellar activity values for HD 77 946 we performed a combined GP, transit, and RV fit to the *TESS* PDCSCAP, the previously decorrelated *CHEOPS* photometry, and the HARPS-N RVs (with the process separately repeated for both the DRS and s-BART data). We used the PYORBIT[4] code (Malavolta et al. 2016, 2018), a package for modelling planetary and stellar activity signals, where best-fitting activity and planet parameters were obtained using the dynamic nested sampling code DYNESTY (Speagle 2020). PYORBIT uses the BATMAN python package (Kreidberg 2015) for fitting the transit to the photometric data, where we assumed a quadratic stellar intensity profile for fitting the limb darkening coefficients, and an exposure time of 120.0 s for the *TESS* observations, and 30.0 s for the *CHEOPS* observations as inputs to the light-curve model. The GP analysis was carried out using a quasi-periodic covariance kernel function as defined in equation (1), which combines a squared exponential and standard periodic kernel (Haywood et al. 2014; Grunblatt, Howard & Haywood 2015). PYORBIT implements this GP quasi-periodic kernel through the GEORGE[5] package (Ambikasaran et al. 2016). The stellar activity parameters obtained in Section 3.3 were used to inform priors for

[3]https://github.com/j-faria/kima

[4]https://github.com/LucaMalavolta/PyORBIT, version 8.

[5]https://github.com/dfm/george

Table 3. Stellar and planetary properties calculated from the combined RV, transit and GP fit. The prior label $\mathcal{N}$ represents a Normal distribution.

Parameter	Description	Priors	HD 77 946 b (DRS RVs)	HD 77 946 b (s-BART RVs)
Stellar parameters				
ρ_* [g/cm^3]	Stellar density	$\mathcal{N}(0.52, 0.1)$	$0.558^{+0.072}_{-0.071}$	$0.558^{+0.072}_{-0.071}$
$C1$ [TESS]	LD coefficient	$\mathcal{N}(0.27, 0.1)$	$0.32^{+0.11}_{-0.10}$	$0.35^{+0.10}_{-0.10}$
$C2$ [TESS]	LD coefficient	$\mathcal{N}(0.30, 0.1)$	$0.34^{+0.10}_{-0.10}$	$0.36^{+0.10}_{-0.10}$
$C1$ [CHEOPS]	LD coefficient	$\mathcal{N}(0.38, 0.1)$	$0.37^{+0.10}_{-0.10}$	$0.33^{+0.09}_{-0.09}$
$C2$ [CHEOPS]	LD coefficient	$\mathcal{N}(0.27, 0.1)$	$0.25^{+0.10}_{-0.09}$	$0.23^{+0.09}_{-0.10}$
s_j	RV jitter		$1.09^{+0.30}_{-0.31}$	$0.91^{+0.30}_{-0.33}$
R_0	RV offset 1		$42546.17^{+0.98}_{-0.97}$	$42451.22^{+0.98}_{-0.97}$
R_1	RV offset 2		$42541.29^{+0.99}_{-1.08}$	$42445.60^{+1.00}_{-1.05}$
Stellar activity parameters				
$P_{\rm rot}$ [d]	Rotational period	$\mathcal{N}(14.0, 2.0)$	$13.37^{+0.34}_{-0.25}$	$13.56^{+0.26}_{-0.28}$
λ [d]	Decay time		$29.49^{+0.35}_{-0.33}$	$29.48^{+0.35}_{-0.33}$
$O_{\rm amp}$	Coherence scale		$0.495^{+0.004}_{-0.003}$	$0.495^{+0.003}_{-0.003}$
$H_{\rm amp}$	Variability amplitude		$2.54^{+0.49}_{-0.42}$	$2.56^{+0.49}_{-0.42}$
Orbital parameters				
P [d]	Orbital period		$6.527282^{+0.000016}_{-0.000021}$	$6.527282^{+0.000015}_{-0.000020}$
$T_{\rm C}$ [BJD-2450000]	Transit centre		$9587.4743^{+0.0014}_{-0.0009}$	$9587.4740^{+0.0013}_{-0.0008}$
T_{14} [h]	Transit duration		$3.289^{+0.341}_{-0.490}$	$3.551^{+0.272}_{-0.324}$
$R_{\rm b}/R_*$	Radius ratio		$0.0194^{+0.0012}_{-0.0011}$	$0.0189^{+0.0011}_{-0.0010}$
b	Impact parameter		$0.577^{+0.133}_{-0.242}$	$0.373^{+0.193}_{-0.231}$
e	Eccentricity		$0.140^{+0.092}_{-0.089}$	$0.233^{+0.064}_{-0.079}$
i [deg]	Inclination		$87.02^{+1.04}_{-0.75}$	$87.79^{+1.31}_{-1.05}$
a/R_*	Semimajor axis ratio		$11.902^{+0.730}_{-0.890}$	$12.009^{+0.650}_{-0.741}$
a [AU]	Semimajor axis		$0.0720^{+0.0012}_{-0.0012}$	$0.0720^{+0.0012}_{-0.0012}$
K [m s^{-1}]	RV semi-amplitude		$2.65^{+0.44}_{-0.45}$	$2.66^{+0.40}_{-0.41}$
Mass, radius, and density				
$M_{\rm b}$ [$M_\oplus$]	Planet mass		$8.48^{+1.46}_{-1.49}$	$8.38^{+1.32}_{-1.32}$
$R_{\rm b}$ [$R_\oplus$]	Planet radius		$2.762^{+0.106}_{-0.097}$	$2.705^{+0.086}_{-0.081}$
$\rho_{\rm b}$ [$\rho_\oplus$]	Planet density		$0.426^{+0.090}_{-0.086}$	$0.450^{+0.085}_{-0.081}$

the GP fit which was performed simultaneously with the combined transit and RV fit.

Inferred stellar and planetary parameters from the combined fit are shown in Table 3, alongside the priors implemented. The prior for $P_{\rm rot}$ is explained in Section 3.3, while the prior on stellar density comes from stellar mass and radius estimates in Section 3.2. The priors placed on the limb-darkening coefficients were calculated using interpolation of table 25 from Claret (2017) for the *TESS* light curves and table 8 from Claret (2021) for the *CHEOPS* light curves. The fit converges to a moderately eccentric planetary orbit, with a posterior on $K_{\rm b}$ corresponding to a $\sim 6\sigma$ detection. Using the estimates for the stellar mass and radius obtained in Section 3.2 and the HARPS-N DRS RVs, we derive that HD 77 946 b has a mass $M_{\rm b} = 8.48^{+1.46}_{-1.49}\,{\rm M}_\oplus$ and a radius $R_{\rm b} = 2.76^{+0.11}_{-0.10}\,{\rm R}_\oplus$.

We also performed the same combined GP, transit, and RV fit using the s-BART RVs, as mentioned in Section 2.2.2, with the resulting inferred stellar and planetary parameters shown in Table 3. In this case the fit converged to a slightly more eccentric planetary orbit than that of the fit with the DRS RVs, which led to a slightly higher posterior on $K_{\rm b}$ corresponding to a $\sim 6.6\sigma$ detection. From this we also derived a slightly lower mass and radius for HD 77 946 b of $M_{\rm b} = 8.38^{+1.32}_{-1.32}\,{\rm M}_\oplus$ and $R_{\rm b} = 2.71^{+0.09}_{-0.08}\,{\rm R}_\oplus$. These results still fall within 1σ of those derived from the HARPS-N DRS RVs, but this does suggest that the choice of data reduction technique can influence the resulting planetary parameters. We favour these results as we find that the fit with the s-Bart RVs gives a stronger detection of the planet's mass and required less jitter in the fit, although there is tension in the derived eccentricity when using either RV data set.

Fig. 5 shows the phase-folded light curves for both the *TESS* and *CHEOPS* data along with the best-fitting transit and GP models for the fit with the s-BART RVs. The left panel of Fig. 6 shows the orbital solution and RV residuals phased on the period of HD 77 946 b. The right panel of Fig. 6 shows the s-BART HARPS-N (filled circles) RVs, together with the corresponding best-fitting model of the planetary signal and the GP model of suspected stellar noise (blue line) as well as its associated uncertainty range (light blue shaded region).

We ensured that the nested sampling was converging to consistent results by running the same model multiple times, and across different machines. Given the aforementioned problems in constraining the stellar rotation period, we also ran models with different priors on $P_{\rm rot}$, although the planetary parameter results were still consistent with 1σ on all runs. A corner plot with all the planetary parameters can be found in Appendix A, see Fig. A2. In addition to this the RV semi-amplitude (2.69 ± 0.57 m s^{-1}) obtained from the SCALPELS analysis in Section 3.3 was combined with the stellar mass and orbital

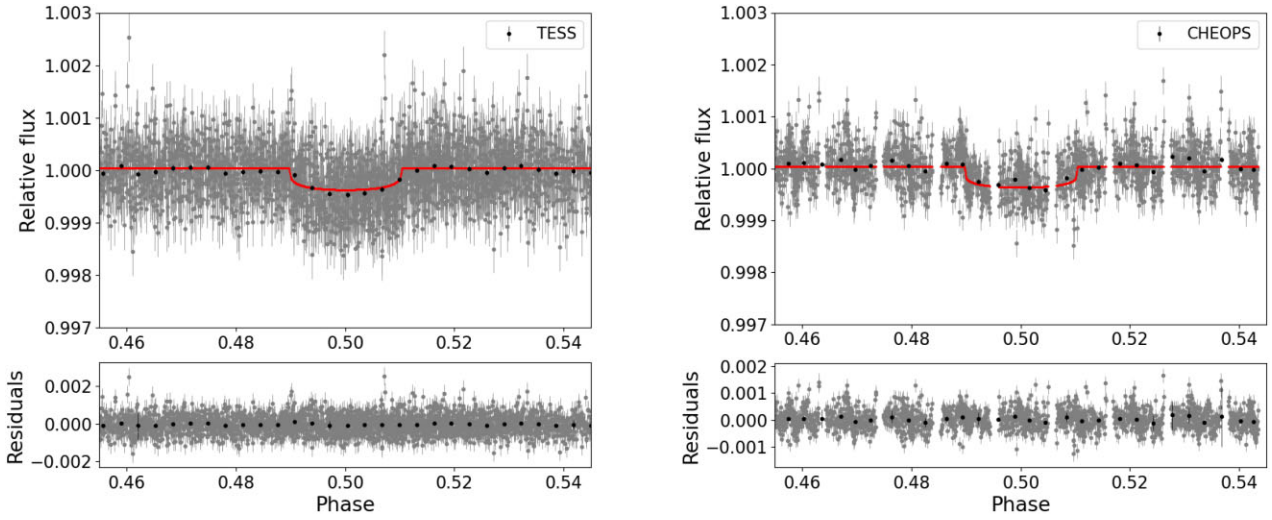

Figure 5. Combined fit results obtained from PYORBIT. Transit fit to the light curve data from *TESS* (*left*) and *CHEOPS* (*right*). The short cadence (2 min for *TESS*, 30 s for *CHEOPS*) fluxes are plotted in grey, the fluxes binned every 30 min are overplotted in black, and the fitted transit is shown by the red solid line.

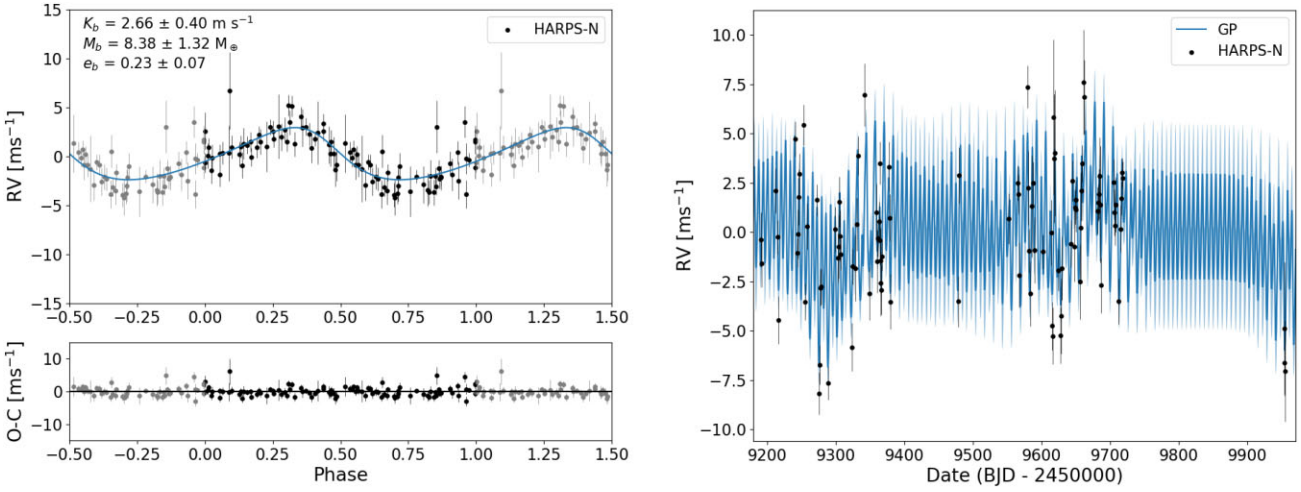

Figure 6. Combined fit results obtained from PYORBIT. *Left*: The RV fit to the HARPS-N s-BART reduced data. The black circular points show the phase-folded HARPS-N RVs, grey points show these same values in subsequent phases, and the blue line shows the best-fitting Keplerian model. *Right*: The RV and GP phase fit to the HARPS-N s-BART reduced data. The black round points show the HARPS-N RVs and the blue lines shows the corresponding GP fit to these data.

inclination (1.17 $M_\odot$ and 87.10 deg, respectively) which lead to a mass determination of 8.83 ± 1.86 $M_\oplus$. This result is consistent with the results from the joint GP, photometric, and spectroscopic fit determined using PYORBIT. Fits were also performed with and without a GP, and comparing the Bayesian Information Criterion (BIC), the non-GP fit had a log-median BIC of −64134 while the fit with a GP had a log-median BIC of −56987. Trotta (2008) suggests under the assumption of a multivariate Gaussian posterior that a log-Bayes factor of >5 should be considered 'strong' evidence for a model. In this case the log-Bayes factor is 3573.5 ($\frac{1}{2}\Delta$BIC), further justifying the use of a GP.

In order to further confirm this, a phase-folded plot of the HARPS-N RVs colour coded to the time period they were taken was produced (see Appendix A Fig. A1). From the grouping of RVs in this plot, we were able to conclude that the results were not being skewed by only sampling some parts of the orbital phase. An additional check was performed to ensure the validity of the eccentricity obtained, in which a one-planet fit was attempted where the planets orbit was forced to be circular (with $e = 0$). From this we calculate a slightly lower mass, $M_b = 7.68^{+1.29}_{-1.25}\,M_\oplus$, corresponding to a similar confidence detection of ∼6σ, with $R_b = 2.83^{+0.07}_{-0.07}\,R_\oplus$. Comparing the BIC, the forced circular orbit had a log-median BIC of −57009 while the eccentric orbit had a log-median BIC of −56987. Thus, while the confidence detections on M_b are both around ∼6σ, the median BIC of the eccentric orbit is better. In addition to this, the log-Bayes factor is 11 ($\frac{1}{2}\Delta$BIC), which supports choosing the more eccentric model. Orbits for single-planet systems are also not typically zero (Van Eylen et al. 2019) and there is no compelling argument to fix the eccentricity of this planet as circular, therefore we favour the model with an eccentric orbit.

The RV time series shown in Fig. 3 also has a hint of a longer term trend. However, as illustrated in Fig. 6, this is captured by the GP in our aforementioned fits as we did not fit for a linear trend. We did carry out some additional model runs allowing for a longer period Keplerian, in addition to the known Keplerian (HD 77 946 b) and a GP. However, these failed to converge on a longer period Keplerian

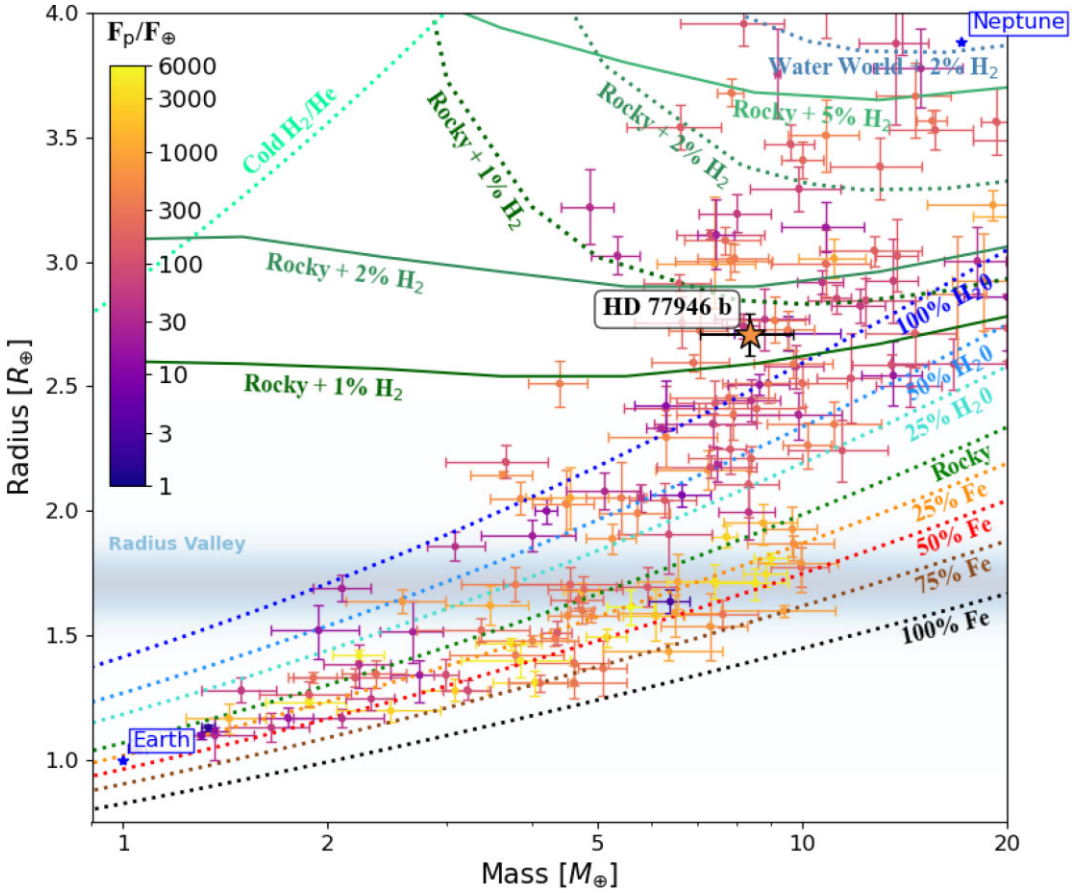

Figure 7. M-R diagram for HD 77 946 b. HD 77 946 b is indicated by the star and other confirmed planets with masses and radii measured to be better than 20 per cent and 10 per cent, respectively, taken from the Extrasolar Planets Encyclopaedia, are also shown. The dotted lines show different planet compositions, taken from Zeng et al. (2019) (1000 K), and the solid lines show compositions taken from Lopez & Fortney (2014) (1 Gyr, solar metallicity and flux of 1000$F_\oplus$). The data points are colour-coded according to their incident flux. Also shown are Earth and Neptune, for reference, and we indicate the approximate location of the radius valley (Fulton et al. 2017).

signal. While this does not mean that we can rule out the presence of a longer period companion, the existing data do not provide support for such a signal. Further RV observations with HARPS-N are ongoing which will allow us to further investigate the possibility of a longer period companion, as the existence of a gas giant in the system could determine the internal composition of the inner sub-Neptune by pebble filtering, modulating the water mass fraction of the planet (Bitsch et al. 2021).

5 DISCUSSION

Our analysis allowed us to estimate the mass of HD 77 946 b with a precision better than 20 per cent, and the radius with a precision better than 10 per cent. Combining the modelled mass and radius, we find the planet density to be $\rho_b = 2.32^{+0.44}_{-0.42}$ g cm^{-3}. We place the mass and radius measurements of HD 77 946 b into context and compare them to composition models in Fig. 7, which shows an M-R plot for small planets ($R < 4\ R_\oplus$ and $M < 20\ M_\oplus$). Confirmed planets, with a mass and radius estimated to a precision better than 20 per cent and 10 per cent, respectively, taken from the Extrasolar Planets Encyclopedia[6] are also shown. Furthermore, the coloured lines in the M-R plot show different compositions, taken from Zeng et al. (2019)[7] (dashed lines) and Lopez & Fortney (2014) (solid lines). We include both models due to the recent conclusion of Rogers et al. (2023) in which it is found that the H/He mass relations in Zeng et al. (2019) are not applicable to planets undergoing atmospheric evolution. There are a range of Zeng et al. (2019) models available dependent on temperature, often incorrectly selected based on the equilibrium temperature of the planet. These models assume constant specific entropy, so should instead be selected based on the temperature of the corresponding specific entropy at 100-bar level in the gas envelope. We include the Zeng et al. (2019) models at 1000 K (based on HD 77 946 b's equilibrium temperature calculated in Section 5.1) in Fig. 7 so that a direct comparison can be made to previous mass–radius studies in the literature, but note that the Lopez & Fortney (2014) models are preferred as the assumption of a constant planet age is made instead of constant specific entropy, which is more suitable for planets undergoing atmospheric mass-loss. As can be seen in Fig. 7, HD 77 946 b is consistent with having a sub-Neptune composition with a H/He atmosphere making up about ∼1 per cent of its mass or with having a water-world composition with a steam atmosphere.

[6] http://www.exoplanet.eu

[7] Models are available online at https://lweb.cfa.harvard.edu/~lzeng/planetmodels.html

5.1 Interior structure

To estimate the internal structure of the planet, we used a Bayesian analysis following the method described in Dorn et al. (2015, 2017), the same method employed to analyse the systems L98-59 (Demangeon et al. 2021), TOI-178 (Leleu et al. 2021), TOI-1064 (Wilson et al. 2022), and ν^2 Lupi (Delrez et al. 2021). Our model assumes that the planet has four layers: an inner core made of iron and sulfur, a mantle of silicate (Si, Mg, and Fe), a water layer, and a gaseous layer made of pure H-He. The equations of state used are from Hakim et al. (2018) (iron core), Haldemann et al. (2020) (water layer), and Sotin, Grasset & Mocquet (2007) (silicate mantle). These three layers constitute the 'solid' part of the planet. The thickness of the pure H-He layer depends on stellar age and irradiation as well as the mass and radius of the solid part (Lopez & Fortney 2014).

Our Bayesian model fits the stellar and planetary observed properties to derive the posterior distributions of the internal structure parameters. The planetary parameters modelled are the mass fractions of each layer, the iron molar fraction in the core, the silicon and magnesium molar fraction in the mantle, the equilibrium temperature, and the age of the planet (equal to the age of the star). Uniform priors are used for these parameters, except for the mass of the gas layer which is assumed to follow a uniform-in-log prior, with the water mass fraction having an upper boundary of 0.5 (Marboeuf et al. 2014; Thiabaud et al. 2014). For more details related to the connection between observed data and derived parameters, we refer to Leleu et al. (2021). Finally, we assumed the Si/Mg/Fe molar ratios of each planet to be equal to the stellar atmospheric values. We note that, as in many Bayesian analyses, the results (presented below) depend to some extent on the choice of the priors, which we selected in accordance with Dorn et al. (2017, 2018) and Leleu et al. (2021).

The result of the internal structure modelling for HD 77 946 b is shown in Fig. 8. The planet shows a relatively small gaseous envelope for a sub-Neptune of $0.02^{+0.04}_{-0.02}$ $M_\oplus$ corresponding to less than 1 per cent of its total mass. However, due to its very high equilibrium temperature (1248^{+40}_{-38} K), the radius of the gas layer is $0.69^{+0.33}_{-0.33}$ $R_\oplus$, which corresponds to one-fourth of the HD 77 946 b's total radius. Compared to the Earth, due to a possibly thick water layer ($0.29^{+0.19}_{-0.26}$), the iron core is proportionally smaller ($0.09^{+0.11}_{0.08}$ mass fraction in HD 77 946 b compared to it being ∼1/3 of the Earth's mass).

The amount of water on the planet is almost unconstrained ($0.29^{+0.19}_{-0.26} M_{\rm solid}$) due to the presence of an atmosphere. As the planet is close to its star we could assume that the planet formed inside the ice-line, that is to say it is a water-poor planet. We tried to model this eventuality by constraining the maximum fraction of water to 10^{-3}. In this case, the envelope mass is bigger ($0.06^{+0.04}_{-0.03}$ $M_\oplus$) in order to retrieve a similar planet density, as well as its radius ($0.96^{+0.24}_{-0.24}$), with the same $M_{\rm core}/M_{\rm mantle}$. Both scenarios are plausible; however we favour the water-rich environment because the water-poor environment requires a strong assumption. Although giving slightly different results, they are both able to describe a planet of this mass and this radius.

5.2 Compositional confusion surrounding sub-Neptunes

As seen in Fig. 7, HD 77 946 b resides in an area on the M-R diagram where a degeneracy exists between the water-world and silicate/iron-hydrogen models. While there have been strong arguments in favour of the existence of water-worlds (Zeng et al. 2019), they cannot be identified based on the mass–radius relationship alone unless we can rule out a significant gas layer (Adams, Seager & Elkins-Tanton 2008). Our interior structure modelling of HD 77 946 b in Section 5.1 concludes that there is a H/He atmosphere that makes up a reasonable fraction of the radius, and the inclusion of both Zeng et al. (2019) and Lopez & Fortney (2014) models in Fig. 7 reinforces this. However, the planet is very hot ($T_{\rm eq}$ ∼ 1250 K) and as this is a highly irradiated planet water may be in supercritical state as shown in Mousis et al. (2020). The interior structure modelling in Section 5.1 does not take into account different states of water, but even in the case of a solid layer of ice water our model still output a high water mass fraction of 30^{+18}_{-26} per cent. Aguichine et al. (2021) show that planets with a water mass fraction between 20 and 50 per cent and irradiation temperatures of ∼1000 K could also explain the location of HD 77 946 b in the M-R diagram.

With an equilibrium temperature of ∼1250 K, it can be seen from Fig. 7 that HD 77 946 b is one of the hottest planets in this region of the M-R diagram. This would indicate that if HD 77 946 b has a H/He atmosphere then it is escaping. Following the mass and radius predictions of Kubyshkina & Fossati (2022), HD 77 946 b resides roughly on the upper boundary of the 1350–1700 K 'migrated scenario', an escape-dominated region of M-R plots. This would indicate that for a H/He atmosphere HD 77 946 b's evolution is mainly shaped by atmospheric escape and that atmospheric loss, due to the planets high thermal energy and low gravity throughout the first few tens of megayears of its evolution, is the dominant mechanism in driving the atmospheric evolution of the planet. While the Lopez & Fortney (2014) grids establish that a 1 per cent H/He atmosphere matches the structure at the planet's current-day size, mass, and irradiation, these models do not include photoevaporation. However, photoevaporation models do predict some sub-Neptunes

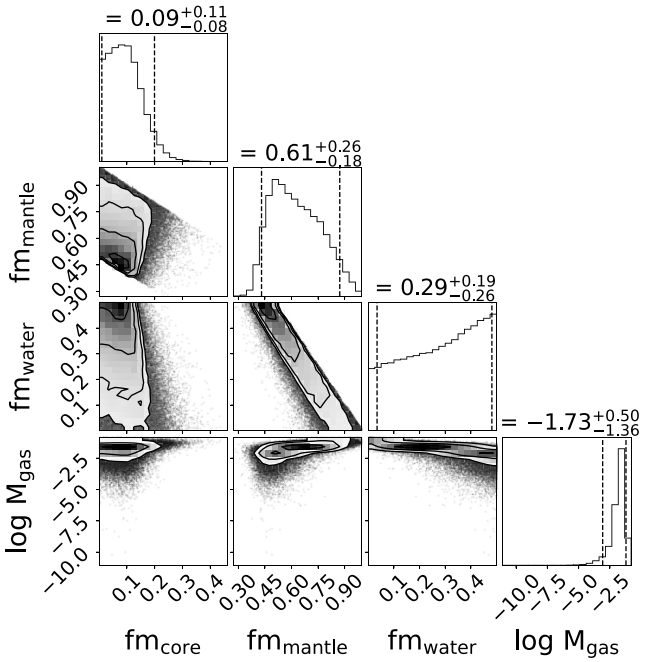

Figure 8. Posterior distributions of the main parameters describing the internal structure of HD 77 946 b. The corner plot shows the mass fraction of the inner core and of the water layer, the molar fractions of silicon and magnesium in the mantle, the iron molar fraction in the inner core, and the mass of gas in logarithmic scale. On top of each column are printed the mean and the 5 per cent and 95 per cent quantiles values.

above the valley at 6 d (Owen & Wu 2017), and although these are on the hotter end of the sub-Neptunes, they are actually expected from population-level photoevaporation models. In addition to this, using the ATES grid from Caldiroli et al. (2022) the predicted lifetime for a 1 per cent H/He atmosphere is 1–3 Gyr. This makes a 1 per cent H/He atmospheric composition entirely reasonable given our estimated age of the system of 3.5 Gyr. In this case, the primordial parameters characterizing the planet play a minor role in HD 77 946 b's location in Fig. 7, as a wide range of possible initial parameters could have lead to the same outcome (Kubyshkina et al. 2018, 2019, 2020). Planets such as this, often called sub-Neptunes, sit above the radius valley, while stripped-core planets which are significantly smaller in size, often called super-Earths, sit below. Further studying larger sub-Neptunes, like HD 77 946 b, will be key to constraining fundamental planetary formation and evolution processes such as atmospheric accretion and escape, migration, and core-composition. Furthermore, the precision of HD 77 946 b's mass measurement means that this key parameter can be considered when endeavouring to understand these planetary pathways, as currently the hydrostatic upper atmospheres of small, low-irradiated exoplanets is mostly unexplored except for the Jeans escape model (Konatham, Martin-Torres & Zorzano 2020).

5.3 Prospects for atmospheric observations

We calculated the transmission spectroscopic metric (TSM) and the emission spectroscopic metric (ESM) outlined in Kempton et al. (2018), for follow-up atmospheric observations with *JWST*, but find that the TSM and ESM (56.81 and 5.63, respectively) do not meet the threshold presented (suggested threshold of TSM > 90 for 1.5 < R_b < 10 $R_\oplus$, and ESM > 7.5). Even though HD 77 946 b may not have a high enough TSM, or ESM, to be amongst the 'best-in-class' targets highlighted by Hord et al. (2023), it still has one of the highest TSMs for a sub-Neptune orbiting a hot star ($T_{\rm eff}$ > 6000 K), as shown in Fig. 9, so is still an interesting target for transmission spectroscopy. However, the brightness of the target, at $K = 7.6$, would saturate many instrument modes on *JWST*, but we emphasize that while this target may not be suitable for *JWST* spectroscopy, a single transit should give a clear detection of the atmosphere if no clouds or hazes were present. We verified this with PandExo models with equilibrium chemistry and no clouds or hazes, and found that G140H (and potentially G235H) would be able to pick up water features in a H/He-dominated atmosphere without fully saturating the instrument, so studies of its atmosphere for other reasons than just spectrum investigations are also viable.

We also looked into the possibility of atmospheric He detection through transmission spectroscopy in the near-infrared. Scaling from Kirk et al. (2022), who constrain the peak helium absorption for WASP-52b (J = 10.5, $T_{14} = 1.8 \sim h$) to 0.31 per cent, for HD 77 946 (J = 7.9, $T_{14} = 3.3 \sim h$) we could expect about 0.07 per cent precision with Keck/NIRSPEC on a similar signal for HD 77946. Thus, detection of a strong metastable He signal would be challenging but perhaps not impossible in multiple transits because of the bright star, given that Zhang et al. (2021) achieved better precision on 55 Cancri e. Still, some caution is warranted as our low $\log(R'_{HK})$ value indicates that HD 77 946 does not exhibit strong chromospheric activity. Planets orbiting stars with $\log(R'_{HK}) \lesssim -5$ are rarely detected to exhibit helium absorption (Bennett et al. 2023), and unfortunately, given the distance (d = 99pc) and this inactivity, Lyman α detection would be challenging due to interstellar absorption.

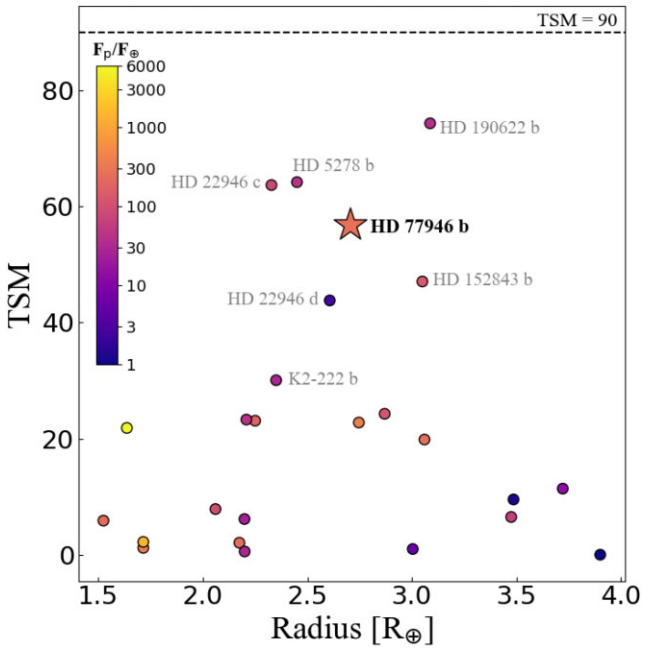

Figure 9. Plot of planetary radius versus TSM for host stars with an effective temperature greater than 6000 K. HD 77946b is indicated by the star and other confirmed planets, taken from the Extrasolar Planets Encyclopedia, are also shown colour-coded by their incident flux. Additionally plotted is the recommended TSM=90 threshold (horizontal dashed line). While there are currently no sub-Neptunes orbiting hot stars that pass this recommended threshold, we note that HD 77 946 b is one of the top five candidates in this area.

5.4 Benefits of *CHEOPS*

The inclusion of photometric light curves from *CHEOPS* improved the precision of our results significantly. In order to quantify this, the model was run a number of times with and without the various sets of data accrued. More specifically the model was run with only the HARPS-N s-BART RVs and sector 21 of the *TESS* data, the HARPS-N s-BART RVs and both *TESS* sectors, the HARPS-N s-BART RVs and sector 47 of the *TESS* data alongside the *CHEOPS* transit this sector overlaps with, the HARPS-N s-BART RVs with both *TESS* sectors and the first *CHEOPS* transit, and lastly the HARPS-N s-BART RVS with both *TESS* sectors and both *CHEOPS* transits. With the inclusion of the first *CHEOPS* transit, the precision on the period and the transit centre time improved significantly (by 31 per cent and 43 per cent, respectively), and with the inclusion of the second *CHEOPS* transit the precision improved even further (by 37 per cent and 55 per cent, respectively, from the *TESS* only values). The precision on these parameters ensures future studies of this planet can be made without much time loss, and while this is not yet possible with the instrumentation on *JWST*, in the future there is potential for this with more sensitive instrumentation. For instance, to plan observations of a transit of HD 77 946 in a decade using the precision on the parameters from the model run with only *TESS* photometric data, the uncertainty on the timing would be ∼28 min. However, adding the *CHEOPS* photometric data to the model means that this uncertainty reduces to only ∼17 min. In addition to the aforementioned parameters, the precision on the planetary radius marginally improves (by 7 per cent) with the inclusion of the *CHEOPS* data, which further highlights the benefits of the ultra-high precision photometry.

6 CONCLUSIONS

In this paper, we present the analysis of the *TESS* target HD 77946, a bright ($V = 9.00$) F5 star ($M_\star = 1.17\ M_\odot$, $R_\star = 1.31\ R_\odot$). Using the results of a HARPS-N GTO campaign, as well as two additional *CHEOPS* transits, alongside the two initial *TESS* campaigns (each lasting around 27 d), we find HD 77 946 to host one small (2.7 $R_\oplus$, 8.4 $M_\oplus$) transiting sub-Neptune, with an orbital period of ∼6.53 d. The accuracy of our mass measurement for this planet allows us to constrain likely composition scenarios. The planet is located above the radius valley, indicating that it is a sub-Neptune, and since the radius valley is theorized to separate super-Earths and sub-Neptunes the composition of the planet can be theorized in this context. We furthermore compare the properties of HD 77946's planet alongside those with similarly constrained radii and masses, and find that these suggest that HD 77 946 b is a sub-Neptune with an iron-core fraction smaller than that of the Earth and an H/He atmosphere that is about ∼1 per cent of the total mass.

This result contributes to the highlighted degeneracy between water-worlds and silicate/iron-hydrogen models. In the case of HD 77 946 b the concept of a water-world remains ambiguous, while both Zeng et al. (2019) and Lopez & Fortney (2014) models suggest the existence of a ∼1 per cent H/He atmosphere, and our own internal composition models indicate that this H/He atmosphere makes up a significant proportion of the radius of the planet, the temperature of the planet means that that water could be in a supercritical state and so a steam atmosphere may be possible. This precise characterization of HD 77 946 b makes it a valuable target for follow-up atmospheric observations to further explore this, as there are not many precisely characterized small planets amenable for atmospheric characterization orbiting stars like the Sun or bigger. Confirming or refuting the existence of water worlds for solar-type stars could have strong implications for our understanding of *Kepler* demographics and our own Solar system. This is also key to gain a better understanding of planetary compositions, which can in turn better inform the processes involved in planetary formation and evolution.

The combination of *TESS*, *CHEOPS*, and HARPS-N data in the characterization of this planet presents a promising approach in the use of multiple data sets from a range of telescopes in the improvement of precision of planetary properties. The addition of multiple transits by two space telescopes combined with 100 + RVs from a ground-based telescope helped to significantly improve the radius and mass precision, placing it among the top 10 mass and radius precision for confirmed F star planetary systems on the Extrasolar Planets Encyclopedia. This is promising for the future, as good sampling of the exoplanet population is needed to further inform planet formation models.

ACKNOWLEDGEMENTS

The HARPS-N project was funded by the Prodex Program of the Swiss Space Office (SSO), the Harvard University Origin of Life Initiative (HUOLI), the Scottish Universities Physics Alliance (SUPA), the University of Geneva, the Smithsonian Astrophysical Observatory (SAO), the Italian National Astrophysical Institute (INAF), University of St. Andrews, Queen's University Belfast, and University of Edinburgh.

We thank Suzanne Aigrain for her work in obtaining observations.

MPi acknowledges the financial support from the ASI-INAF Addendum n.2018-24-HH.1-2022 'Partecipazione italiana al Gaia DPAC – Operazioni e attività di analisi dati'.

ACC and TW acknowledge support from STFC consolidated grant numbers ST/R000824/1 and ST/V000861/1, and UKSA grant number ST/R003203/1. KR acknowledges support from STFC Consolidated grant number ST/V000594/1.

AAJ acknowledges support from a World-Leading St Andrews Doctoral Scholarship.

This work has been carried out within the framework of the NCCR PlanetS supported by the Swiss National Science Foundation under grants 51NF40_182901 and 51NF40_205606.

RDH is funded by the UK Science and Technology Facilities Council (STFC)'s Ernest Rutherford Fellowship (grant number ST/V004735/1).

FPE would like to acknowledge the Swiss National Science Foundation (SNSF) for supporting research with HARPS-N through the SNSF grants nr. 140649, 152721, 166227, and 184618. The HARPS-N Instrument Project was partially funded through the Swiss ESA-PRODEX Programme.

This work has been carried out within the framework of the NCCR PlanetS supported by the Swiss National Science Foundation under grants 51NF40_182901 and 51NF40_205606. This project has received funding from the European Research Council (ERC) under the European Union's Horizon 2020 research and innovation programme (grant agreement SCORE No 851555).

This research has made use of data obtained from or tools provided by the portal exoplanet.eu of The Extrasolar Planets Encyclopaedia.

DATA AVAILABILITY

This paper includes raw data collected by the *TESS* mission, which are publicly available from the Mikulski Archive for Space Telescopes (MAST, https://archive.stsci.edu/tess). Raw data collected by *CHEOPS* can be found using the file keys in Table 1 at https://cheops-archive.astro.unige.ch/archive_browser/. Observations made with HARPS-N on the Telescopio Nazionale Galileo 3.6m telescope are available in Appendix B.

REFERENCES

Adams E. R., Seager S., Elkins-Tanton L., 2008, ApJ, 673, 1160
Aguichine A., Mousis O., Deleuil M., Marcq E., 2021, ApJ, 914, 84
Ambikasaran S., Foreman-Mackey D., Greengard L., Hogg D. W., O'Neil M., 2016, IEEE Trans. Pattern Anal. Mach. Intell., 38, 252
Anna John A. et al., 2023, MNRAS, 525, 1687
Anna John A., Collier Cameron A., Wilson T. G., 2022, MNRAS, 515, 3975
Asplund M., Grevesse N., Sauval A. J., Scott P., 2009, ARA&A, 47, 481
Bailer-Jones C. A. L., Rybizki J., Fouesneau M., Demleitner M., Andrae R., 2021, AJ 161 147
Bennett K. A., Redfield S., Oklopčić A., Carleo I., Ninan J. P., Endl M., 2023, AJ, 165, 264
Bensby T., Feltzing S., Lundström I., 2003, A&A, 410, 527
Bensby T., Feltzing S., Oey M. S., 2014, A&A, 562, A71
Benz W. et al., 2021, Exp. Astron., 51, 109
Bitsch B., Raymond S. N., Buchhave L. A., Bello-Arufe A., Rathcke A. D., Schneider A. D., 2021, A&A, 649, L5
Boisse I., Bouchy F., Hébrard G., Bonfils X., Santos N., Vauclair S., 2011, A&A, 528, A4
Bonfanti A. et al., 2021, A&A, 646, A157
Brown A. G. A. et al., 2021, A&A, 650, C3
Buchhave L. A. et al., 2012, Nature, 486, 375
Buchhave L. A. et al., 2014, Nature, 509, 593
Caldiroli A., Haardt F., Gallo E., Spinelli R., Malsky I., Rauscher E., 2022, A&A, 663, A122
Cannon A. J., Pickering E. C., 1918, Henry Draper Catalogue and Extension 1, Harv. Ann, 91

Chen D.-C. et al., 2021, ApJ, 909, 115
Claret A., 2017, A&A, 600, A30
Claret A., 2021, Res. Notes Am. Astron. Soc., 5, 13
Collier Cameron A. et al., 2019, MNRAS, 487, 1082
Collier Cameron A. et al., 2021, MNRAS, 505, 1699
Cosentino R. et al., 2012, in McLean I. S., Ramsay S. K., Takami H., eds, Proc. SPIE Conf. Ser. Vol. 8446, Ground-based and Airborne Instrumentation for Astronomy IV. SPIE, Bellingham, p. 84461V
Cosentino R. et al., 2014, in Ramsay S. K., McLean I. S., Takami H., eds, Proc.SPIE Conf. Ser. Vol. 9147, Ground-based and Airborne Instrumentation for Astronomy V. SPIE, Bellingham, p. 2658
Cutri R. M. et al., 2003, 2MASS All Sky Catalog of point sources.
David T. J. et al., 2021, AJ, 161, 265
Delrez L. et al., 2021, Nat. Astron., 5, 775
Demangeon O. D. S. et al., 2021, A&A, 653, A41
Dorn C., Khan A., Heng K., Connolly J. A. D., Alibert Y., Benz W., Tackley P., 2015, A&A, 577, A83
Dorn C., Mosegaard K., Grimm S. L., Alibert Y., 2018, ApJ, 865, 20
Dorn C., Venturini J., Khan A., Heng K., Alibert Y., Helled R., Rivoldini A., Benz W., 2017, A&A, 597, A37
Dotter A., 2016, ApJS, 222, 8
Dotter A., Chaboyer B., Jevremović D., Kostov V., Baron E., Ferguson J. W., 2008, ApJS, 178, 89
Dumusque X. et al., 2021, A&A, 648, A103
Egeland R., Soon W., Baliunas S., Hall J. C., Pevtsov A. A., Bertello L., 2017, ApJ, 835, 25
Faria J. P. et al., 2022, A&A, 658, A115
Faria J. P., Santos N. C., Figueira P., Brewer B. J., 2018, J. Open Source Softw., 3, 487
Fulton B. J. et al., 2017, AJ, 154, 109
Fulton B. J., Petigura E. A., 2018, AJ, 156, 264
Gaia Collaboration, 2023, A&A, 674, A1
Ginzburg S., Schlichting H. E., Sari R., 2018, MNRAS, 476, 759
Grunblatt S. K., Howard A. W., Haywood R. D., 2015, ApJ, 808, 127
Guerrero N. M. et al., 2021, ApJS, 254, 39
Gupta A., Schlichting H. E., 2019, MNRAS, 487, 24
Hakim K., Rivoldini A., Van Hoolst T., Cottenier S., Jaeken J., Chust T., Steinle-Neumann G., 2018, Icarus, 313, 61
Haldemann J., Alibert Y., Mordasini C., Benz W., 2020, A&A, 643, A105
Haywood R. D. et al., 2014, MNRAS, 443, 2517
Ho C. S. K., Eylen V. V., 2023, MNRAS, 519, 4056
Høg E. et al., 2000, A&A, 355, L27
Hojjatpanah S. et al., 2020, A&A, 639, A35
Hord B. J. et al., 2023, preprint (arXiv:2308.09617)
Hoyer S., Guterman P., Demangeon O., Sousa S. G., Deleuil M., Meunier J. C., Benz W., 2020, A&A, 635, A24
Jenkins J. M. et al., 2016, in Chiozzi G., Guzman J. C., eds, Proc. SPIE Conf. Ser. Vol. 9913, Software and Cyberinfrastructure for Astronomy IV. SPIE, Bellingham, p. 99133E
Johnson D. R. H., Soderblom D. R., 1987, AJ, 93, 864
Kempton E. M.-R. et al., 2018, PASP, 130, 114401
Kirk J., Dos Santos L. A., López-Morales M., Alam M. K., Oklopčić A., MacLeod M., Zeng L., Zhou G., 2022, AJ, 164, 24
Konatham S., Martin-Torres J., Zorzano M.-P., 2020, Proc. R. Soc. A, 476, 20200148
Koval V. V., Marsakov V. A., Borkova T. V., 2009, Astron. Rep., 53, 1117
Kreidberg L., 2015, PASP, 127, 1161
Kubyshkina D. et al., 2018, A&A, 619, A151
Kubyshkina D. et al., 2019, ApJ, 879, 26
Kubyshkina D., Fossati L., 2022, A&A, 668, A178
Kubyshkina D., Vidotto A. A., Fossati L., Farrell E., 2020, MNRAS, 499, 77
Kurucz R., 1993, ATLAS9 Stellar Atmosphere Programs and 2 km/s grid. Kurucz CD-ROM No. 13. Cambridge, p. 13
Lacedelli G. et al., 2022, MNRAS, 511, 4551
Leleu A. et al., 2021, A&A, 649, A26
Lindegren L. et al., 2021, A&A, 649, A4
Lopez E. D., Fortney J. J., 2014, ApJ, 792, 1
Luque R., Pallé E., 2022, Science, 377, 1211
Malavolta L. et al., 2016, A&A, 588, A118
Malavolta L. et al., 2018, AJ, 155, 107
Mamajek E. E., Hillenbrand L. A., 2008, ApJ, 687, 1264
Marboeuf U., Thiabaud A., Alibert Y., Cabral N, Benz W., 2014, A&A, 570, A36
Maxted P. F. L. et al., 2022, MNRAS, 514, 77
Mayor M. et al., 2003, The Messenger, 114, 20
Mortier A. et al., 2020, MNRAS, 499, 5004
Mortier A., Faria J. P., Correia C. M., Santerne A., Santos N. C., 2015, A&A, 573, A101
Mortier A., Santos N. C., Sousa S. G., Fernandes J. M., Adibekyan V. Z., Delgado Mena E., Montalto M., Israelian G., 2013, A&A, 558, A106
Mortier A., Sousa S. G., Adibekyan V. Z., Brandão I. M., Santos N. C., 2014, A&A, 572, A95
Morton T. D., 2015, Astrophysics Source Code Library, record ascl:1503.010
Mousis O., Deleuil M., Aguichine A., Marcq E., Naar J., Aguirre L. A., Brugger B., Gonçalves T., 2020, ApJ, 896, L22
Nava C. et al., 2022, AJ, 163, 41
Nava C., López-Morales M., Haywood R. D., Giles H. A. C., 2020, AJ, 159, 23
Nesterov V. V., Kuzmin A. V., Ashimbaeva N. T., Volchkov A. A., Röser S., Bastian U., 1995, A&AS, 110, 367
Noyes R. W., Hartmann L. W., Baliunas S. L., Duncan D. K.,Vaughan A. H. , 1984a, ApJ, 279, 763
Noyes R. W., Weiss N. O., Vaughan A. H., 1984b, ApJ, 287, 769
Osborn H. P. et al., 2022, A&A, 664, A156
Owen J. E., Wu Y., 2013, ApJ, 775, 105
Owen J. E., Wu Y., 2017, ApJ, 847, 29
Perryman M. A. C. et al., 1997, A&A, 323, L49
Petigura E. A. et al., 2022, AJ, 163, 179
Press W. H., Teukolsky S. A., Vetterling W. T., Flannery B. P., 1992, Numerical Recipes in FORTRAN. The Art of Scientific Computing. Cambridge Univ. Press, Cambridge
Rajpaul V., Aigrain S., Osborne M. A., Reece S., Roberts S., 2015, MNRAS, 452, 2269
Reddy B. E., Lambert D. L., Allende Prieto C., 2006, MNRAS, 367, 1329
Ricker G. R. et al., 2014, J. Astron. Telesc. Instrum. Syst., 1, 014003
Rogers J. G., Schlichting H. E., Owen J. E., 2023, ApJ, 947, L19
Rogers L. A., Seager S., 2010, ApJ, 712, 974
Sandoval A., Contardo G., David T. J., 2021, ApJ, 911, 117
Serrano L. M. et al., 2022, A&A, 667, A1
Silva A. M. et al., 2022, A&A, 663, A143
Sneden C. A., 1973, PhD thesis, The University of Texas at Austin
Sotin C., Grasset O., Mocquet A., 2007, Icarus, 191, 337
Sousa S. G., 2014, ARES + MOOG: A Practical Overview of an Equivalent Width (EW) Method to Derive Stellar Parameters. Springer International Publishing, p. 297
Sousa S. G., Santos N. C., Adibekyan V., Delgado-Mena E., Israelian G., 2015, A&A, 577, A67
Sousa S. G., Santos N. C., Israelian G., Lovis C., Mayor M., Silva P. B., Udry S., 2011, A&A, 526, A99 +
Speagle J. S., 2020, MNRAS, 493, 3132
Stassun K. G. et al., 2018, AJ, 156, 102
Stock S. et al., 2020, A&A, 643, A112
Suárez Mascareño A., Rebolo R., González Hernández J. I., Esposito M., 2017, MNRAS, 468, 4772
Thiabaud A., Marboeuf U., Alibert Y., Cabral N, Leya I., Mezger K., 2014, A&A, 562, A27
Trotta R., 2008, Contemp. Phys., 49, 71
V. Rajpaul, , et al., 2021, MNRAS,507,1847–1868
Van Eylen V. et al., 2019, AJ, 157, 61
Van Eylen V., Agentoft C., Lundkvist M. S., Kjeldsen H., Owen J. E., Fulton B. J., Petigura E., Snellen I., 2018, MNRAS, 479, 4786
Wilson T. G. et al., 2022, MNRAS, 511, 1043
Wilson, T. G. et al., ., 2024, in review
Wright E. L. et al., 2010, AJ, 140, 1868
Zeng L. et al., 2019, Proc. Natl. Acad. Sci., 116, 9723
Zeng L. et al., 2021, ApJ, 923, 247
Zhang M., Knutson H. A., Wang L., Dai F., Oklopcic A., Hu R., 2021, AJ, 161, 181

APPENDIX A: ADDITIONAL FIGURES

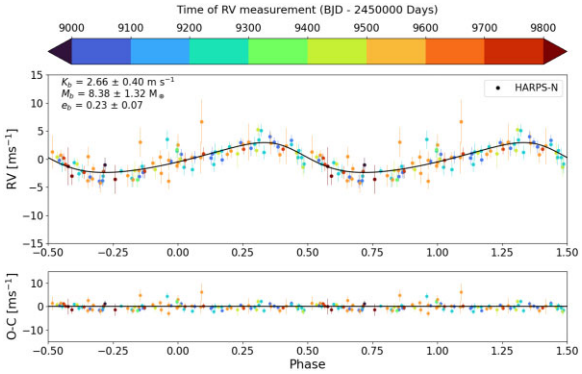

Figure A1. The RV fit to the s-BART reduced HARPS-N data colour coded by the time period the observation was taken. The black line shows the best-fitting Keplerian model.

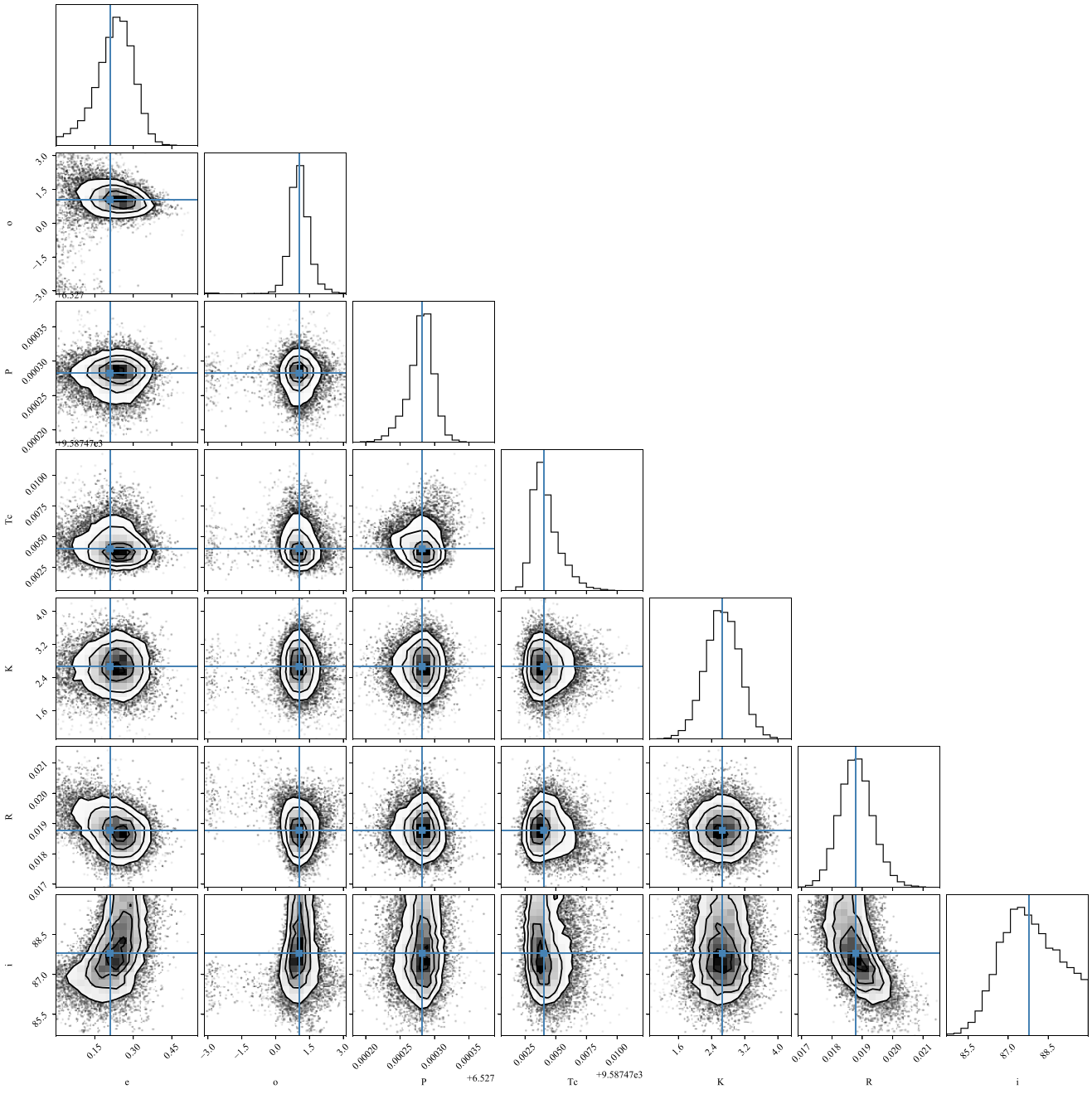

Figure A2. Corner plot of the best-fitting planetary parameters obtained from the combined transit and s-BART RV fit.

APPENDIX B: RV DATA TABLES

Table B1. HARPS-N radial velocity data and activity indicators (DRS 2.3.5).

BJD_{UTC} (d)	RV ($m\ s^{-1}$)	σ_{RV} ($m\ s^{-1}$)	BIS_{span} ($m\ s^{-1}$)	$\sigma_{BIS_{span}}$ ($m\ s^{-1}$)	FWHM ($km\ s^{-1}$)	σ_{FWHM} ($km\ s^{-1}$)	Hα	$\sigma_{H\alpha}$	$\log R'_{HK}$	$\sigma_{\log R'_{HK}}$
2459190.738244	42545.63	1.43	22.64	2.88	7.89579	0.00288	0.190614	0.000198	−5.00992	0.00243
2459191.726875	42544.71	1.30	18.37	2.60	7.88572	0.00260	0.188756	0.000133	−4.99872	0.00192
2459212.579407	42547.40	1.16	21.49	2.32	7.88992	0.00232	0.187651	0.000108	−5.00220	0.001670
2459215.700791	42546.76	0.91	22.53	1.81	7.88838	0.00181	0.189548	0.000083	−4.99492	0.001054
2459216.701496	42542.55	1.27	16.67	2.54	7.88784	0.00254	0.192039	0.000152	−5.01565	0.001934
2459240.688690	42551.90	0.91	19.73	1.83	7.88491	0.00183	0.187665	0.000072	−4.99512	0.001110
2459244.615700	42545.98	0.74	18.82	1.49	7.88567	0.00149	0.191498	0.000082	−5.00989	0.000746
2459245.626303	42546.28	1.30	21.83	2.61	7.89188	0.00261	0.188959	0.000156	−5.00007	0.001999
2459246.628068	42548.00	1.47	20.14	2.94	7.88453	0.00294	0.188186	0.000176	−5.02032	0.002631
2459247.649564	42550.13	1.09	21.21	2.19	7.88688	0.00219	0.192860	0.000147	−4.98634	0.001353
2459253.634872	42551.17	1.06	22.19	2.12	7.88977	0.00212	0.185250	0.000089	−5.00296	0.001462
2459255.632035	42543.04	0.97	17.94	1.94	7.88397	0.00194	0.188543	0.000091	−4.99380	0.001182
2459258.707176	42548.39	1.19	14.96	2.38	7.88617	0.00238	0.188371	0.000131	−5.02338	0.001902
2459272.479370	42548.17	0.84	21.08	1.68	7.88774	0.00168	0.190507	0.000087	−5.00828	0.000922
2459275.535218	42539.73	1.10	22.52	2.20	7.89072	0.00220	0.189822	0.000128	−5.01908	0.001554
2459276.547869	42537.89	1.04	19.77	2.07	7.89502	0.00207	0.189724	0.000122	−5.01309	0.001352
2459277.511019	42542.46	0.98	23.18	1.97	7.88923	0.00197	0.189613	0.000115	−4.99725	0.001206
2459278.542373	42544.62	0.96	18.90	1.93	7.89235	0.00193	0.188118	0.000104	−5.00032	0.001137
2459289.510242	42538.21	0.88	23.75	1.75	7.88770	0.00175	0.187647	0.000083	−4.99339	0.000967
2459299.526078	42546.04	1.20	23.63	2.39	7.89351	0.00239	0.185450	0.000112	−5.01840	0.001815
2459303.509382	42543.54	1.31	23.79	2.61	7.88904	0.00261	0.187090	0.000118	−5.00778	0.002149
2459304.475734	42545.88	1.71	18.16	3.43	7.88886	0.00343	0.185810	0.000198	−5.00684	0.003292
2459305.468367	42546.94	1.34	21.28	2.67	7.89100	0.00267	0.186004	0.000128	−4.99559	0.002097
2459306.554217	42545.53	1.32	24.82	2.64	7.90420	0.00264	0.186187	0.000161	−4.99972	0.002103
2459307.460545	42545.04	0.82	21.70	1.65	7.89597	0.00165	0.186539	0.000062	−4.98568	0.000862
2459323.484332	42541.54	1.27	20.53	2.54	7.88360	0.00254	0.187299	0.000156	−5.00107	0.001955
2459324.415964	42544.93	0.95	18.37	1.90	7.88709	0.00190	0.189235	0.000104	−4.99814	0.001124
2459328.486578	42543.98	1.74	21.94	3.49	7.89026	0.00349	0.188016	0.000196	−5.00685	0.00363
2459330.548136	42546.86	1.35	18.70	2.70	7.89051	0.00270	0.182204	0.000132	−4.99043	0.00235
2459332.497322	42550.91	1.04	20.95	2.08	7.88630	0.00208	0.182855	0.000086	−4.97477	0.00135
2459342.427322	42551.28	1.72	26.78	3.43	7.88266	0.00343	0.182009	0.000137	−5.02066	0.00396
2459343.439367	42556.16	2.04	24.80	4.07	7.88516	0.00407	0.180045	0.000184	−5.03492	0.00515
2459344.463297	42557.58	1.35	21.65	2.70	7.89582	0.00270	0.178534	0.000104	−5.00018	0.00248
2459345.464621	42556.06	1.30	22.83	2.60	7.89100	0.00260	0.182092	0.000097	−4.99065	0.00239
2459349.385292	42542.09	1.37	17.52	2.75	7.89782	0.00275	0.184820	0.000144	−4.97997	0.00220
2459359.374662	42547.11	1.57	13.99	3.14	7.88737	0.00314	0.181396	0.000151	−5.00339	0.00293
2459360.401225	42544.94	1.66	19.12	3.31	7.88807	0.00331	0.186620	0.000156	−5.04058	0.00362
2459361.378805	42544.74	0.94	21.42	1.87	7.89241	0.00187	0.184807	0.000089	−4.99773	0.00114
2459363.379202	42549.07	1.01	18.51	2.03	7.88823	0.00203	0.189136	0.000115	−4.98885	0.00129
2459364.379400	42549.12	1.11	20.17	2.23	7.89459	0.00223	0.183737	0.000126	−4.99346	0.00157
2459364.445783	42545.19	1.26	19.49	2.52	7.88835	0.00252	0.182185	0.000138	−5.00053	0.00213
249365.3897683	42544.38	1.77	16.04	3.55	7.90140	0.00355	0.188554	0.000239	−5.01815	0.00379
2459365.452059	42543.30	1.69	20.25	3.38	7.89046	0.00338	0.187437	0.000201	−5.02172	0.00386
2459366.394436	42543.29	1.32	21.51	2.63	7.89258	0.00263	0.189100	0.000150	−4.98859	0.00215
2459367.380219	42545.28	0.74	22.26	1.48	7.89265	0.00148	0.190189	0.000078	−4.99028	0.00072
2459377.372865	42548.58	1.30	18.26	2.60	7.89079	0.00260	0.182648	0.000132	−4.98786	0.00206
2459378.374164	42546.63	1.21	19.16	2.42	7.89463	0.00242	0.181863	0.000124	−4.98886	0.00183
2459379.372684	42542.83	1.48	18.81	2.96	7.89083	0.00296	0.177918	0.000160	−4.98670	0.00252
2459478.754516	42542.05	1.35	21.39	2.70	7.89219	0.00270	0.191788	0.000141	−4.99190	0.00226
2459479.750471	42550.05	1.46	20.17	2.91	7.88647	0.00291	0.188824	0.000135	−4.99578	0.00257
2459551.637860	42540.76	1.34	20.88	2.68	7.87728	0.00268	0.195722	0.000200	−4.96282	0.00220
2459565.648685	42543.86	0.90	19.76	1.80	7.87775	0.00180	0.193419	0.000106	−4.99928	0.00118
2459566.603313	42543.09	1.02	17.98	2.05	7.87859	0.00205	0.195089	0.000125	−4.98415	0.00147
2459567.772083	42539.51	1.68	22.61	3.36	7.87449	0.00336	0.190469	0.000218	−4.99283	0.00362
2459579.695802	42549.13	1.09	19.57	2.19	7.88275	0.00219	0.193077	0.000128	−4.97463	0.00162
2459580.670788	42541.77	1.95	18.34	3.91	7.88148	0.00391	0.195502	0.000322	−4.95991	0.00420
2459581.666799	42538.54	1.10	22.15	2.20	7.88110	0.00220	0.195271	0.000133	−4.96425	0.00162
2459583.635824	42540.33	1.65	20.28	3.30	7.87606	0.00330	0.192377	0.000224	−4.98113	0.00347
2459585.703278	42542.86	2.68	23.96	5.36	8.87764	0.00536	0.194946	0.000395	−5.06381	0.00925
2459587.697808	42543.45	1.09	20.65	2.18	7.87787	0.00218	0.192123	0.000137	−5.01491	0.00176
2459589.646447	42538.63	1.71	22.66	3.43	7.87687	0.00343	0.189918	0.000222	−4.98076	0.00366
2459601.661063	42539.88	0.88	20.03	1.75	7.87323	0.00175	0.191366	0.000082	−4.97205	0.00107
2459614.590547	42539.93	1.78	19.43	3.56	7.87874	0.00356	0.195972	0.000314	−5.00648	0.00398

Table B1 – *continued*

BJD_{UTC} (d)	RV ($m\ s^{-1}$)	σ_{RV} ($m\ s^{-1}$)	BIS_{span} ($m\ s^{-1}$)	$\sigma_{BIS_{span}}$ ($m\ s^{-1}$)	FWHM ($km\ s^{-1}$)	σ_{FWHM} ($km\ s^{-1}$)	Hα	$\sigma_{H\alpha}$	$\log R'_{HK}$	$\sigma_{\log R'_{HK}}$
2459615.707950	42536.50	1.26	24.59	2.52	7.87274	0.00252	0.194392	0.000186	−4.98889	0.00220
2459616.609675	42536.43	1.45	21.23	2.91	7.87942	0.00291	0.189195	0.000152	−4.97938	0.00280
2459617.446595	42544.01	4.30	32.76	8.41	7.88332	0.00841	0.184741	0.000621	−5.32254	0.03471
2459618.627553	42545.10	4.36	21.56	6.93	7.87238	0.00693	0.189146	0.000508	−5.17112	0.01786
2459619.568840	42541.27	3.42	8.780	6.84	7.86571	0.00684	0.187352	0.000499	−5.10429	0.01492
2459624.617176	42540.10	1.08	21.86	2.15	7.87520	0.00215	0.193279	0.000131	−4.99474	0.00166
2459627.630534	42536.75	1.43	20.21	2.86	7.88350	0.00286	0.191854	0.000191	−4.99546	0.00276
2459628.639713	42537.72	1.98	21.46	3.96	7.87955	0.00396	0.190605	0.000261	−5.01533	0.00527
2459629.667599	42541.17	1.59	28.67	3.19	7.88230	0.00319	0.188325	0.000178	−5.00543	0.00362
2459642.508152	42539.36	1.20	24.17	2.39	7.87693	0.00239	0.189119	0.000135	−4.99967	0.00199
2459644.596920	42544.26	1.05	20.74	2.09	7.87951	0.00209	0.190071	0.000104	−4.98704	0.00155
2459647.532098	42539.93	1.81	28.89	3.62	7.86876	0.00362	0.192875	0.000238	−5.01207	0.00419
2459648.495016	42542.60	0.88	19.67	1.76	7.88071	0.00176	0.189947	0.000082	−4.95548	0.00105
2459649.456712	42543.15	1.17	18.72	2.34	7.87702	0.00234	0.189671	0.000128	−4.97015	0.00183
2459649.485986	42542.42	1.00	19.22	2.00	7.88329	0.00200	0.193279	0.000115	−4.96934	0.00137
2459655.586609	42537.04	1.91	21.64	3.81	7.87221	0.00381	0.193593	0.000257	−5.00888	0.00484
2459656.579639	42537.05	2.90	21.05	5.80	7.87132	0.00580	0.191036	0.000430	−5.10786	0.01208
2459658.575254	42540.11	1.50	23.21	3.01	7.88011	0.00301	0.191272	0.000193	−5.00224	0.00314
2459659.593557	42544.49	0.92	18.34	1.84	7.87490	0.00184	0.188337	0.000115	−4.98032	0.00123
2459661.590946	42542.86	2.76	7.005	5.52	7.87246	0.00552	0.187074	0.000367	−5.03862	0.00951
2459662.543021	42544.09	1.92	17.34	3.84	7.87734	0.00384	0.187936	0.000236	−5.00167	0.00465
2459681.484604	42543.80	1.20	21.39	2.41	7.88442	0.00241	0.191549	0.000151	−4.99980	0.00202
2459682.470313	42544.09	0.94	18.47	1.88	7.87994	0.00188	0.186032	0.000083	−4.96822	0.00122
2459683.458239	42544.47	1.30	19.13	2.61	7.87934	0.00261	0.190440	0.000135	−4.99794	0.00238
2459684.457695	42543.91	1.99	23.69	3.97	7.88790	0.00397	0.186930	0.000261	−5.03925	0.00544
2459685.487443	42547.75	3.13	30.14	6.26	7.88418	0.00626	0.186686	0.000466	−5.07349	0.01237
2459686.495470	42540.80	1.43	24.38	2.86	7.87533	0.00286	0.189690	0.000173	−4.99259	0.00277
2459705.397453	42546.40	1.21	21.76	2.42	7.87375	0.00242	0.192274	0.000151	−4.97071	0.00183
2459706.358644	42543.39	1.19	18.78	2.38	7.88012	0.00238	0.191660	0.000151	−4.97177	0.00187
2459707.386372	42543.58	1.02	21.00	2.04	7.88241	0.00204	0.190483	0.000116	−4.97150	0.00141
2459708.408500	42543.11	1.39	19.23	2.78	7.87579	0.00278	0.189700	0.000158	−4.99957	0.00272
2459712.392219	42540.32	1.18	19.75	2.36	7.87731	0.00236	0.190551	0.000140	−4.98207	0.00190
2459715.401979	42541.48	1.23	20.88	2.47	7.88239	0.00247	0.195684	0.000197	−5.04080	0.00234
2459716.404532	42544.99	0.87	21.27	1.74	7.87171	0.00174	0.190347	0.000094	−4.98060	0.00107
2459717.404407	42545.85	0.75	18.86	1.51	7.87379	0.00151	0.188707	0.000067	−4.98103	0.00083
2459718.410118	42545.62	0.89	14.11	1.78	7.87559	0.00178	0.187069	0.000089	−4.96388	0.00108
2459953.507204	42535.22	3.63	26.95	7.26	7.87150	0.00726	0.192918	0.000584	−5.16967	0.01880
2459953.596313	42532.62	1.65	25.41	3.30	7.87617	0.00396	0.194549	0.000254	−4.99257	0.00334
2459954.680378	42533.91	2.66	22.81	5.32	7.86896	0.00532	0.190955	0.000396	−4.98334	0.00724

Table B2. HARPS-N radial velocity data (s-BART).

BJD_{UTC} (d)	RV ($m\ s^{-1}$)	σ_{RV} ($m\ s^{-1}$)
2459190.738244	42450.83	1.38
2459191.726875	42449.65	1.23
2459212.579407	42453.33	1.13
2459215.700791	42450.97	0.87
2459216.701496	42446.76	1.20
2459240.688690	42455.95	0.87
2459244.615700	42450.18	0.71
2459245.626303	42451.12	1.25
2459246.628068	42452.99	1.39
2459247.649564	42454.18	1.03
2459253.634872	42456.65	1.02
2459255.632035	42447.69	0.94
2459258.707176	42451.51	1.16
2459272.479370	42452.85	0.81
2459275.535218	42443.03	1.06
2459276.547861	42444.50	0.99
2459277.511019	42448.39	0.93
2459278.542373	42448.47	0.92
2459289.510242	42443.57	0.85
2459299.526078	42451.37	1.16
2459303.509382	42449.92	1.25
2459304.475734	42450.49	1.61
2459305.468367	42452.76	1.27
2459306.554217	42451.03	1.30
2459307.460545	42450.09	0.78
2459323.484332	42445.39	1.22
2459324.415963	42449.48	0.92
2459328.486578	42449.40	1.68
2459330.548136	42451.62	1.34
2459332.497322	42455.09	1.01
2459342.427323	42458.18	1.61
2459343.439367	42458.79	1.90
2459344.463297	42461.02	1.28
2459345.464621	42461.64	1.23
2459349.385292	42448.10	1.34
2459359.374662	42452.21	1.48
2459360.401225	42449.75	1.60
2459361.378805	42450.90	0.91
2459363.379202	42451.75	0.99
2459364.379401	42454.72	1.09
2459364.445783	42450.80	1.23
2459365.389768	42449.77	1.68
2459365.452059	42448.63	1.64
2459366.394436	42448.30	1.26
2459367.380219	42449.98	0.71
2459377.372865	42454.54	1.26
2459378.374164	42451.95	1.19
2459379.372684	42447.69	1.40
2459478.754516	42447.71	1.31
2459479.750471	42454.10	1.42
2459551.637860	42446.28	1.26
2459565.648685	42448.10	0.89
2459566.603313	42447.51	0.99
2459567.772083	42443.43	1.66
2459579.695802	42452.97	1.07
2459580.670788	42447.86	1.88
2459581.666799	42444.65	1.09
2459583.635824	42442.48	1.64
2459585.703278	42446.91	2.57
2459587.697808	42448.09	1.08
2459589.646447	42444.70	1.67
2459601.661063	42444.61	0.87
2459614.590547	42445.58	1.68
2459615.707950	42440.85	1.22
2459616.609675	42440.34	1.43
2459617.446595	42451.43	3.94
2459618.627553	42449.33	3.27
2459619.568840	42449.62	3.21
2459624.617176	42443.68	1.06
2459627.630534	42440.36	1.43
2459628.639713	42441.35	1.90
2459629.667599	42443.76	1.60
2459642.508152	42445.03	1.18
2459644.596920	42448.21	1.03
2459647.532098	42444.88	1.77
2459648.495016	42446.86	0.87
2459649.456712	42446.76	1.16
2459649.485986	42447.25	1.00
2459655.586609	42443.09	1.89
2459656.579639	42445.82	2.80
2459658.575254	42447.69	1.51
2459659.593557	42449.08	0.93
2459661.590946	42453.21	2.66
2459662.543021	42452.45	1.88
2459681.484604	42446.69	1.20
2459682.470313	42447.09	0.93
2459683.458239	42447.54	1.28
2459684.457695	42448.46	1.93
2459685.487443	42447.01	2.96
2459686.495470	42442.90	1.40
2459705.397452	42448.11	1.20
2459706.358644	42446.60	1.16
2459707.386372	42445.93	1.00
2459708.408500	42446.99	1.39
2459712.392220	42442.09	1.16
2459715.401979	42445.76	1.19
2459716.404532	42447.31	0.86
2459717.404407	42448.64	0.74
2459718.410118	42448.34	0.86
2459953.507204	42440.70	3.40
2459953.596313	42438.99	1.58
2459954.680378	42438.55	2.55

[1]*Institute for Astronomy, University of Edinburgh, Royal Observatory, Blackford Hill, Edinburgh EH9 3HJ, UK*
[2]*Centre for Exoplanet Science, University of Edinburgh, Edinburgh EH9 3HJ, UK*
[3]*SUPA School of Physics and Astronomy, University of St Andrews, North Haugh, St Andrews KY16 9SS, UK*
[4]*Centre for Exoplanet Science, University of St Andrews, North Haugh, St Andrews KY169SS, UK*
[5]*School of Physics and Astronomy, University of Birmingham, Edgbaston, Birmingham B15 2TT, UK*
[6]*Physics Institute, University of Bern, Gesellsschaftstrasse 6, CH-3012 Bern, Switzerland*
[7]*Center for Space and Habitability, University of Bern, Gesellsschaftstrasse 6, CH-3012 Bern, Switzerland*
[8]*DTU Space, National Space Institute, Technical University of Denmark, Elektrovej 328, DK-2800 Kgs. Lyngby, Denmark*
[9]*Dipartimento di Fisica e Astronomia 'Galileo Galilei,' Universitá di Padova, Vicolo del l'Osservatorio 3, I-35122 Padova, Italy*
[10]*Center for Astrophysics | Harvard & Smithsonian, 60 Garden Street, Cambridge, MA 02138, USA*
[11]*Département d'astronomie de l'Université de Genève, Chemin Pegasi 51, CH-1290 Versoix, Switzerland*

[12]*Space sciences, Technologies and Astrophysics Research (STAR) Institute, University of Liège, Allée du 6 Août 19C, B-4000 Liège, Belgium*
[13]*Observatoire de Genève, University of Geneva, Chemin Pegasi 51, CH-1290 Versoix, Switzerland*
[14]*Mullard Space Science Laboratory, University College London, Holmbury St Mary, Dorking, Surrey RH5 6NT, UK*
[15]*INAF - Osservatorio Astronomico di Palermo, Piazza Del Parlamento 1, I-90134 Palermo, Italy*
[16]*Fundación Galileo Galilei - INAF, Rambla J. A. F. Perez, 7, E-38712 S.C. Tenerife, Spain*
[17]*Astrophysics Group, University of Exeter, Exeter EX4 2QL, UK*
[18]*Astrophysics Group, Cavendish Laboratory, University of Cambridge, J.J. Thomson Avenue, Cambridge CB3 0HE, UK*
[19]*INAF - Osservatorio Astrofisico di Torino, Via Osservatorio 20, I-10025 Pino Torinese, Italy*
[20]*Department of Physics and Kavli Institute for Astrophysics and Space Research, Massachusetts Institute of Technology, Cambridge, MA 02139, USA*

This paper has been typeset from a TEX/LATEX file prepared by the author.